Advanced Powder Technology 34 (2023) 104199

Contents lists available at ScienceDirect

Advanced Powder Technology

journal homepage: www.elsevier.com/locate/apt

Image processing of computed tomography scanned poly-dispersed beds for computational fluid dynamic studies

Stylianos Kyrimis [a,b], Robert Raja [b], Lindsay-Marie Armstrong [a,*]

[a] School of Engineering, University of Southampton, SO17 1BJ, UK
[b] School of Chemistry, University of Southampton, SO17 1BJ, UK

ARTICLE INFO

Article history:
Received 22 June 2023
Received in revised form 28 July 2023
Accepted 8 August 2023

Keywords:
Computational fluid dynamics (CFD)
Poly-dispersed catalytic beds
Fixed bed chemical reactors
Computed-tomography (CT) scans
Image processing

ABSTRACT

Achieving our emission reduction goals requires the bulk production of carbon-neutral fuels and chemicals, which are catalytically produced through heterogeneous fixed bed chemical reactors. To optimise and scale-up these reactors, accurate and validated Computational Fluid Dynamics (CFD) models are crucial. Of especial importance to CFD simulations is the accurate depiction of the 3D bed structure used during the experimental setup. A direct one-to-one coupling between experiments and simulations can be achieved by scanning the experimental bed using computed tomography and reconstructing the scanned images as a 3D geometry for CFD simulations. However, processing of the scanned images is necessary to minimise highly coarse features that could impact the overall mesh size. A highly poly-dispersed lab-scale fixed bed reactor, previously scanned and analysed, is processed using various image-processing operations. Depending on the number and the crudeness of the processing operations, the bed is progressively deformed, which impacts both its porosity and its interparticle pore connectivity. The impact of image-processing becomes more evident when the hydrodynamic behaviour, i.e., X-, Y-, and Z-velocity and static pressure, of the beds is explored. CFD simulations revealed highly heterogeneous flow profiles, with the maximum velocity reached being 16-times higher than the average superficial velocity within the bed. Moreover, small modifications in local topological features introduce significant changes to the flow profiles, while the 3D pore interconnectivity was seen to play an equally important role as the interparticle porosity. A particle size study revealed that large particles form less interconnected networks with higher pore volumes, which significantly reduce the flow velocity and the pressure drop experienced by the flow. The generated results yield key insights towards a deeper understanding of the behaviour of fixed bed chemical reactors, highly valuable for catalyst and reactor engineering.

1. Introduction

The net-zero greenhouse gas (GHG) emission reduction target set for 2050 is based on heavily reducing the anthropogenic emissions from various sectors [1,2]. The transportation sector is one of the key contributors of GHG emissions, accounting for 7.98 Gt of CO_2 in 2022 [3]. While vehicle electrification is expected to reduce some of these emissions, heavy-duty road transport, maritime transport, and aviation are expected to continue their dependence on liquid hydrocarbon fuels [2,4], due to their high energy density and compatibility with existing infrastructure. Thus, an alternative emission reduction strategy is the bulk production of carbon-neutral fuels or fuel additives, such as methanol or dimethyl ether [4]. These are predominantly catalytically produced through heterogeneous fixed bed chemical reactors [5-7]. As a result, optimising the design of these reactors for efficient process operation is associated with significant economic and environmental benefits.

Fixed bed chemical reactors are formed by an array of randomly distributed catalytic particles [7], with the final bed structure affecting all aspects of heat and mass transfer phenomena [8,9]. Optimising their design is a multidisciplinary study spanning both the chemistry and the chemical engineering fields, and involving the catalyst type, the catalytic particles sizes and forms, and the operating procedure. Understanding their behaviour requires either extensive demonstration-scale experimental setups or theoretical investigations. For the latter, Computational Fluid Dynamics (CFD) models have been widely used to investigate fixed bed chemical reactors [8-10], due to their ability to replicate the catalytic bed structure and its impact on the resolving flow profiles.

* Corresponding author.
E-mail address: L.Armstrong@soton.ac.uk (L.-M. Armstrong).

https://doi.org/10.1016/j.apt.2023.104199

Nomenclature

Symbols	Meaning, Units
$\vec{g}$	Gravitational acceleration, [m/s^2]
P	Pressure, [Pa]
$\vec{v}_f$	Velocity of the fluid phase, [m/s]
Greek symbols	**Meaning, Units**
ρ_f	Density of the fluid phase, [kg/m^3]
τ	Stress tensor, [Pa]

Abbreviations	Meaning, Units
CFD	Computational Fluid Dynamics, [–]
CT	Computed Tomography, [–]
DEM	Discrete Element Method, [–]
PNM	Pore Network Model, [–]
PR	Particle Resolved, [–]

The accuracy of CFD models is directly coupled to their ability in reproducing the experimental setup, especially the 3D fixed bed geometry. This coupling has been primarily achieved through synthetically generated beds, where the bed structure is generated computationally using the Discrete Element Method (DEM), and the individual particles are then resolved [9,11-13]. With this method, particles of arbitrary shapes are dropped inside cylindrical containers, and their final deposition depends on the mechanical and collisional forces acted upon each particle during the loading process [9,12].

Synthetically generated fixed beds of mono-dispersed spherical particles have been widely studied in the literature [13], allowing particle-resolved CFD (PR-CFD) models to reveal the interconnected nature between the bed structure and its hydrodynamic (i.e., flow velocity and pressure drop) profile. Shin identified that changing the flow direction within the same mono-dispersed spherical bed could affect the permeability experienced by the flow [14]. As a result, the bed's permeability is not only the result of its structural morphology but also of flow-dependent geometric properties, such as the tortuosity of the medium [14]. Zhou *et al.* showed through mono-dispersed spherical beds the impact of particle size on the pressure drop experienced by the medium, with smaller particles exhibiting higher pressure drops and temperatures compared to larger particles, but their exposed surface area was greatly increased [15]. Das *et al.* generated mono-dispersed spherical beds, with the reactor-to-particle diameter ratio, referred to as N-ratio, ranging from 4 to 16, to study the impact of the bed structure on velocity, pressure drop, and heat transfer [16]. At low Reynolds number flows, heat transfer is primarily governed by conduction, while as the Reynolds number increases, convection becomes the dominant heat transfer mechanism [16]. Based on their data, they proposed theoretical correlations for the pressure drop and heat transfer within the bed [16]. Bai *et al.* experimentally investigated the pressure drop within packed beds of spherical or cylindrical particles, using both a laboratory-scale (153 particles) and a plant-scale (up to 1545 particles) reactor [17]. Through DEM, these reactors were also synthetically generated and used with a CFD solver, allowing the investigation of the flow profiles through the packed bed structure [17]. To reduce the computational demands, only a small section of the industrial-scale reactor was chosen, while to generate a good quality computational mesh, the catalytic particles were globally shrunk by 0.5% or 1% for spheres and cylinders, respectively. Through comparison of the CFD results with the experimental data, they identified the sensitivity of the pressure drop to the bed structure, as even a 10% deviation between the experimental and computational bed could lead to a 30% deviation in the pressure drop [17].

PR-CFD models have also expanded into studying more complex particle shapes, such as cylinders, Raschig rings, oblates, prolates, trilobes and many more [18-24]. Such comparative studies increased our understanding of how particle shape affects the flow profiles within the bed. By comparing cylindrical particles and Flatted rings, Tabib *et al.* identified that, due to particle orientations, Flatted rings exhibited smaller pressure drops and higher heat and mass transfer coefficients [25]. Chang *et al.* compared packed beds formed by spheres, oblates and prolates, for their heat transfer characteristics, expressed through the Nusselt number [22]. At high interparticle porosities, the Nusselt number of both the oblate and the prolate beds was larger than that of the spherical bed; however, at lower porosities and low Reynolds number flows, the Nusselt number of the spherical bed becomes larger than that of the oblate bed but remains smaller than that of the prolate bed [22]. Furthermore, they observed that non-isotropic particles can improve mixing within the bed [22]. Pavlišič *et al.* examined the pressure drop of four particle shapes, including spheres and cylinders [26]. They observed that particle orientation had a significant impact on the pressure drop and on the tortuosity of the bed [26]. Rodrigues *et al.* investigated the impact of the particle's sphericity on the bed's interparticle porosity and tortuosity using 10 different particle shapes with varying morphological characteristics [27]. For the range of porosity (0.3–0.4) and sphericity (0.65–1.0) considered, they observed that particle sphericity has a considerable impact on the bed's tortuosity, which is comparable to that of the bed's interparticle porosity [27]. Karthik and Buwa evaluated the impact of six particle shapes on pressure drop, temperature profiles, and chemical performance for four chemical reactions [28]. The external surface area, governed by the particle shape, had a linear relationship with the pressure drop, the effectiveness factor, and the reactant conversion, and an inverse relationship with the temperature of the particle [28]. Based on these observations, they determined the optimal particle shape for each of the four reactions by maximising the ratio of reactant conversion to pressure drop [28].

Poly-dispersity, a term referring to particles within the bed having a range of sizes and/or shapes, has also been introduced in DEM-generated beds [29,30]. Zhang *et al.* generated a poly-dispersed packed bed of cylindrical particles, by introducing a gaussian distribution to the particle sizes, and compared the bed structure to that of a mono-dispersed cylindrical bed [29]. They observed that the poly-dispersed bed had larger bulk porosities, i.e., being more loosely packed, compared to the mono-dispersed bed [29]. Furthermore, the radial porosity profile of the two beds was similar in the near-wall region but deviated closer to the bed centre, as the poly-dispersed bed did not present any significant oscillations there [29]. The generated poly-dispersed bed was then used as a geometry for CFD simulations. The flow field around the particles was highly heterogeneous, with local velocity magnitudes being around 13-times higher than the inlet velocity [29]. Boccardo *et al.* generated mono- and poly-dispersed beds of spheres, cylinders, and trilobes, and compared their bed structure (for spheres and cylinders) to those predicted by theoretical correlations [30]. Compared to spheres and cylinders, the radial porosity of the trilobe bed had no periodicity in its profile, instead presenting random oscillations [30]. The poly-dispersed spherical bed was used as a CFD geometry for the solution of the momentum equation. Due to the irregular deposition of particles, inhomogeneous flow fields were observed, with large local velocity gradients [30].

While valuable, synthetically generated beds are an ideal, albeit accurate, representation of actual catalytic beds. They are produced by assuming that particle-particle and particle-reactor wall collisions are always elastic [20,31,32], and are thus prone to small errors when compared to experimental setups. Alternatively, imaging methods, such as Magnetic Resonance Imaging (MRI) and Computed-Tomography (CT), offer a direct coupling between experimental reactors and CFD simulations. They produce a non-invasive depiction and mapping of the catalytic bed, which can then be generated as a 3D geometry and meshed for CFD simulations. MRI detects heterogeneities in the flow physical parameters, e.g., mixture density, within the interparticle network [33], thus MRI literature studies primarily focus on identifying the flow profiles through the pores. Baker *et al.* used 3D MRI on a cylindrical particle bed and implemented the generated geometry onto CFD simulations [34]. The observed pressure drop between the experimental and computational results was close, while any differences between the two can be attributed to the errors introduced by meshing the MRI geometry [34]. Mantle *et al.* combined 3D MRI and MRI velocimetry with Lattice-Boltzmann simulations to investigate the flow field through a packed bed of alumina particles [35]. Due to the heterogeneous nature of the bed structure, the observed flow field was highly irregular, with 40% of the fluid flowing through 10% of the pores [35]. Alternatively, X-Ray CT offers a depiction of the internal structure of an object through 2D projections [36]. Packed bed analysis with CT has focused on describing porosity profiles or characterising the interparticle network connectivity [31,37-39]. Through CT scans, Zhang *et al.* characterised the internal structure of five mono-dispersed cylindrical beds, each formed by changing the packing process by applying different levels of tapping and/or vibration [40]. Compared to mono-dispersed spherical beds, cylindrical beds had a higher bulk porosity, attributed to the local orientation of individual particles [40]. The authors highlighted that local pores created as a result of particle orientations could introduce flow heterogeneities within the bed [40].

Both synthetically generated and image-based geometries are inevitably susceptible to errors introduced by meshing. Meshing is the process of discretising the geometry into smaller computational volumes, referred to as computational cells, which then act as flow resolution volumes. Consequently, high mesh quality is crucial for accurate CFD results. A key topic in all PR-CFD studies is contact region treatment, referring to the contact points, lines, or areas formed between neighbouring particles and between the particles and the wall [41]. Contact regions should be carefully treated to avoid heavily skewed computational cells which reduce the local mesh quality and lead to computational errors and convergence issues [25,41,42]. Various methods have been employed in the literature to deal with them, which include either global methods, i.e., global particle shrinkage [17,24,25,28,42,43], also referred to as "gaps" method, or local methods, i.e., locally flattening the particle [29,44-47], i.e., "caps" method, or bridging neighbouring particles in the contact region [25,26,30,44,45], i.e., "bridges" method. Through comparative studies, both Wehinger *et al.* [18] and Dixon *et al.* [48] agree that global treatment methods introduce considerable errors and should thus be replaced by local treatment methods which better respect and preserve the porosity of the fixed bed. Otherwise, with the pressure drop being highly sensitive to the bed's porosity, significant deviations with the experimental results could be observed [48]. Image-based methods involve additional processing steps prior to mesh generation, which include image thresholding and particle segmentation [34,49-51]. Specifically, through black-white image thresholding, the scanned images are binarized and the boundaries between particles and background are distinguished. Then, particle segmentation separates neighbouring particles thus resolving the contact regions with a process similar to the "caps" method. As is the case with the synthetically-generated beds, both processing steps introduce local topological errors which should be minimised [13,34].

All these studies are indicative of the complex interactions between particle shapes and orientations and the heat and mass transfer characteristics, especially in poly-dispersed beds. With the bed structure being the predominant driver of all aspects of flow profiles, accurately depicting it on CFD models is key. In our previous study, the internal structure of six experimental fixed beds used for ethanol dehydration was mapped through CT [52]. Their poly-dispersed nature was identified, as the catalytic particles that formed them, produced by sieving, exhibited a wide range of sizes, shapes, and orientations [52]. Furthermore, it was observed that dust particles, i.e., particles smaller than 100 μm, were present in large numbers within the catalytic beds, attributed to particle fracturing during the loading process. However, increasing the number of sieving passes greatly reduced the population of dust particles [52]. An image sample of the quintuple sieved 300–500 μm bed of our previous work [52] is presented in Fig. 1. It can be seen that, due to particle fragmentation, the boundaries between some particles and the background space are blurred, and the images appear "dirty" because of the existence of dust particles. Consequently, meshing such local topological complexities, present within the entire bed volume, could lead to exhaustive computational demands, while also generating computational errors and instabilities due to poor local mesh quality. In our follow-up study, we identified that, for the 300–500 μm case, a 10% sample section can be a suitable representative of the full bed, as the bulk and radial porosity were reasonably reproduced [53]. However, for the 500–700 μm case, due to its large heterogeneity, a 50% section would be better suited compared to a 10% section. Subsequently, a mesh independency study was completed for the 300–500 μm bed [53]. Here, four different image-processing methods to clean the produced CT-scans were tested. With the goal of accurately preserving the bed geometry while reducing the computational demands, the different methods were evaluated based on their impact on the bed structure, i.e., bulk, radial, and axial porosity and interparticle pore network, as well as on the resulting flow profiles. Specifically, prior to meshing, the produced images were cleaned through various operations,

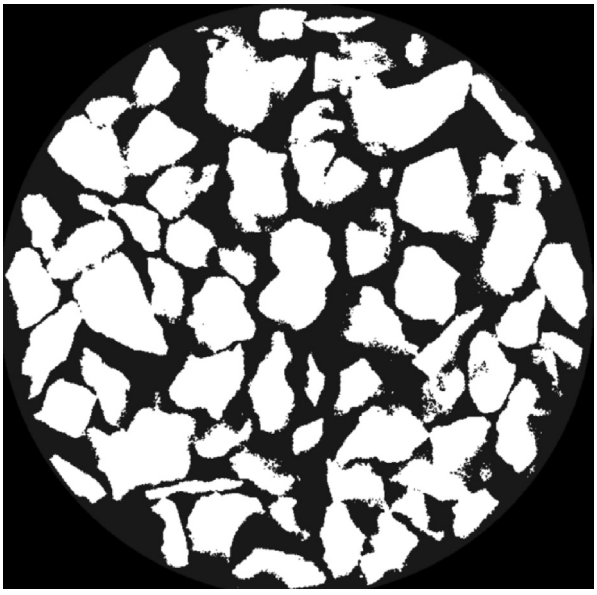

Fig. 1. Binary CT-scanned image of the quintuple-sieved 300–500 μm bed, produced from our full bed characterisation study [52].

such as "Erode", "Dilate", "Fill Holes", and "Close", and the bed structure they form is then compared to that of the original, unprocessed bed. Subsequently, the errors introduced by meshing are estimated, and the hydrodynamic flow profiles within the bed, i.e., velocity and pressure drop, are explored. Finally, by comparing the flow profiles produced by the 300–500 and the 500–700 μm cases, the impact of the particle size on the flow velocity and pressure drop was quantified. With image-based tools offering a direct coupling between experiments and simulations, they offer unique new aspects in the field of CFD studies. However, the development of delicate pre-processing methods to clean the produced images and preserve the topological features are key to take advantage of these methods.

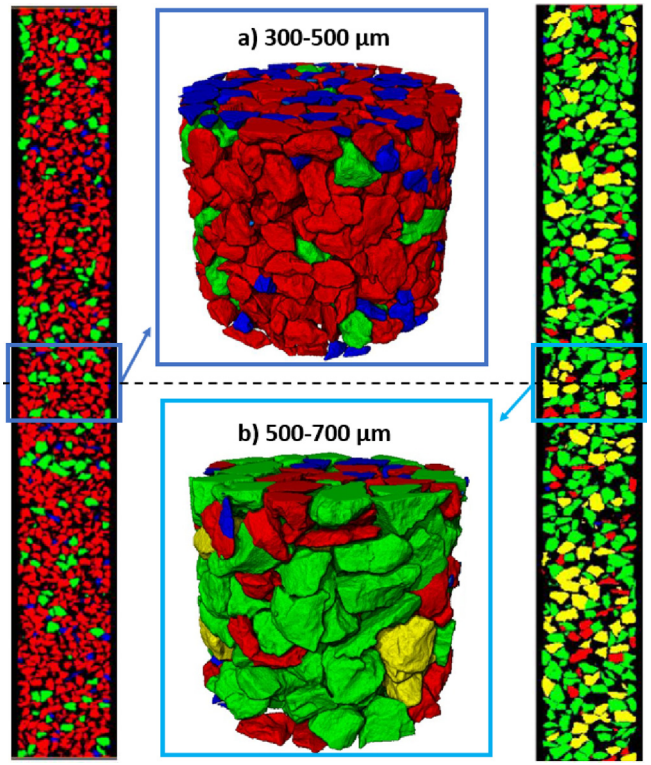

Fig. 2. 10% sample sections of the a) 300–500 and b) 500–700 μm full quintuple-sieved beds of our previous work [52]. Particle colours indicate their equivalent diameter metric, with blue: 100–300 μm, red: 300–500 μm, green: 500–700 μm, and yellow: >700 μm. (For interpretation of the references to colour in this figure legend, the reader is referred to the web version of this article.)

2. Methodology

The experimental reactor setup was described in our previous work [52] and is repeated in Figure A1 of the ESI. Building on from our previous investigation [53], a 10% sample section of the full bed is considered for all cases presented here. This bed section spans equally upwards and downwards from the exact centre of the 300–500 and the 500–700 μm beds, as seen in Fig. 2. While this section is representative of the full 300–500 μm bed geometry, in terms of radial and bulk porosities, it is not representative of the full 500–700 μm bed [53]. For validation purposes of the produced CFD flow results with experimental data, a larger bed section would be required. However, comparing the flow profiles within the two beds will produce valuable results for how the particle size affects the hydrodynamic, i.e., velocity and pressure, characteristics. Validation with experimental data is instead planned for our future work.

2.1. Pre-processing

In our previous work [52], two separate software were used to characterise the packed bed structure, Fiji ImageJ [54] and Amira/Avizo (ThermoFisher Scientific). The former was used to binarize the produced images, using a thresholding separation, and to measure the porosity characteristics through the "Analyze Particles" function. The latter was used to produce a 3D geometry from the scanned images, using particle segmentation, and to measure their 3D dimensions. Consequently, only the bare minimum processing was used to preserve the bed structure and prevent introducing large errors. Here, however, to clean and mesh the original CT-scans, the dust particles should be removed. For this purpose, four different operations offered by Fiji ImageJ [54] were considered. These are the "Erode", "Dilate", "Fill holes", and "Close" operations, and the effects they introduce are showcased in Table 1. Specifically, "Erode" removes pixels from the edges of binary images, while "Dilate" adds pixels [54]. "Fill holes" connects binary objects that are surrounded by elements with the same threshold value, while "Close" sequentially performs a "Dilate" and an "Erode" operation [54].

By combining these processes, four different test cases are generated, ranging in the level of processing involved. The first test case, TC-0, included two processing operations, "Erode" followed by "Dilate". In the next two test cases, TC-1 and TC-2, processing increased to include a third subsequent operation following "Erode" and "Dilate", specifically "Fill holes" and "Close", respectively. Finally, a crude method to process the produced images was also considered, which, after the initial "Erode" and "Dilate" operations, involved a double "Erosion" and a double "Dilation" operation. This test case is referred to as TC-3. For comparative purposes, the original CT-images will also be considered as a test

Table 1
Image-processing methods offered by Fiji ImageJ [54] and considered in this work.

Image-processing methods offered by Fiji ImageJ [54]		
Process	**Result**	**Method description**
Original image	Image processing	Binary image
Erode	Image processing	Removes pixels from the edges of objects
Dilate	Image processing	Adds pixels to the edges of objects
Fill holes	Image processing	Connects objects by filling surrounded elements
Close	Image processing	Performs a dilation followed by an erosion operation

Table 2
Test cases produced based on the image-processing method used to clean the original CT-scanned images.

CT-scanned image-processing	
Test case	**Operation**
TC-Original	No processing – Original CT-scanned images from [52]
TC-0	Erode, and Dilate operations
TC-1	Erode, Dilate, Fill holes operations
TC-2	Erode, Dilate, Close operations
TC-3	Erode, Dilate, Erode (x2), Dilate (x2)

case, referred to as TC-Original. These test cases, along with their pre-processing operations, are all presented and described in Table 2.

The porosity of all five test cases was characterised with Fiji ImageJ, following the same process described in our previous work [52] and repeated here. For the radial porosity, concentric rings, produced from the centre of the bed, fragmentised the bed section into radial slices with a radial thickness of 0.05 mm. These rings create a radial area along the height of the bed, e.g., radial area in-between the radial distance of 2.0 mm and 1.95 mm from the bed centre. In these rings, the "Analyze Particles" operation from Fiji ImageJ [54] is used, which measures the total area covered by the particles and compares it to the total area of the concentric rings, thus evaluating the packing density (corresponding to 1 – porosity). For the bulk and axial porosities, the total particle area in each CT-scanned image is evaluated through the "Analyze Particles" operation, i.e., without utilising the concentric rings, and the packing density is then integrated either through the entire bed section (bulk porosity) or through smaller regions with axial lengths of 0.05 (axial porosity).

2.2. Characterising the interparticle network

The Amira-Avizo software includes the Pore Network Model (PNM), which is a method capable of quantifying the pore sizes within the interparticle space. PNM is based on the watershed algorithm (WA) [55]; initially, a distance map is formed within the interparticle space which allows for the determination of the geometric location farthest away from any neighbouring particles, i.e., the pore centre. Subsequently, the watershed basins surrounding the pore centre are identified, and the pore is segmented from its neighbours [55,56]. The contact surfaces between two neighbouring pores are connected through throats, and the surface area and volume of the pore is then measured [55-57]. To take advance of the PNM, the binary CT-images were reversed, thus the interparticle space appeared as the area of interest. Then, in a process similar to Fernando *et al.* [39], an "Axis connectivity" module, followed by a pore "Segmentation" module, created a labelled image, where each pore is distinguished and separated from its neighbour. The "Segmentation" module uses a combination of distance mapping, H-maxima, and watershed to separate the various pore regions [39,58]. Finally, the pore network is generated and quantified. The metrics used to characterise the pores are the pore volume and the coordination number, i.e., the number of interconnected pore neighbours.

2.3. Meshing

Prior to meshing the different test case geometries, empty regions were added before and after the catalytic bed, with a length of 0.6 and 1.8 mm, respectively. The section prior to the bed will allow the flow to naturally develop before reaching the catalytic bed, while the section after the bed will prevent any backflow effects originating from the outlet of the reactor to affect the flow [59]. In our previous work, we noticed that backflow effects are limited to the near-outlet region, i.e., to a height of up to 0.8 mm from the outlet, and do not penetrate deeper into the porous medium [59]. Consequently, expanding the geometry by a 1.8 mm-length empty region should be sufficient to prevent any backflow interference. The length needed prior to the bed for the flow to develop is usually lower [60], so its length was chosen as 1/3rd that of the past-bed region. The goal of this work is to evaluate the errors introduced by different image-processing methods to the bed geometry, and thus to its hydrodynamic profile. Consequently, the catalytic particles themselves are neglected, instead being treated as void regions within the geometry. These will be included in our future work, where heat and mass transfer, as well as intraparticle physicochemical phenomena (i.e., diffusion and reaction), within the poly-dispersed beds will be investigated.

Meshing of the different test cases was performed with the Simpleware ScanIP software from Synopsys Inc, which has been used in the literature to produce meshes from image-based geometries [34,51]. Prior to meshing, further processing was done with Simpleware, using the "Island Removal" operation, which removed unconnected particles that were smaller than 60 μm, thus further ensuring the removal of dust particles. Meshing was then performed with the +FE Free algorithm, which uses adaptive tetrahedral cells, utilising small cell sizes around regions with complex topological features within the porous medium, and large cell sizes for the free flow regions [51]. Refinement in Simpleware works by setting the coarseness level of the +FE Free algorithm. The coarseness level directly controls the size of the computational elements. Here, the coarsest settings were used, as those were described in the mesh independency study of our previous work [53], performed on TC-2. Specifically, three mesh refinement levels were chosen, with the coarse, medium, and refined settings leading to an average cell size of $4.5e^{-15}$, $2.6e^{-15}$, and $2.2e^{-15}$ m^3, producing a mesh size of 11.0 M, 18.8 M, and 22.3 M cells, respectively. While the coarsest settings do not produce a mesh independent case for TC-2, they are significantly computationally cheaper while also producing an acceptable error (1.6% for velocity and 6.9% for pressure) [53]. Consequently, it is a reasonable simplification to compare the flow profiles within the different test cases while keeping the computational resources to manageable levels. To treat contact regions and generate the mesh, Simpleware segments particles from their neighbours, thus producing results similar to the "caps" method.

Mesh quality is determined by three metrics, orthogonal quality, skewness, and aspect ratio [61,62]. Orthogonal quality refers to the local topology and orthogonality of the computational cells, varying between 1.0 and 0.0, with values closer or equal to 1.0 being desirable [61]. Aspect ratio refers to the stretching of the computational cell, with large ratios causing more deformed cells [61]. It ranges between 1 and 100, with values closer to 1.0 being desirable [61,62]. Skewness is the difference between the shape of a computational cell and the shape of an equilateral cell of equivalent volume [61]. It ranges between 1.0 and 0.0, however, with skewness, values closer to 0.0 are desirable [61,62].

2.4. Computational fluid dynamics (CFD) setup

The hydrodynamic profiles of the produced geometries were resolved using the double precision ANSYS Fluent v22.2 CFD solver. A mass-flow inlet was defined at the top of the geometry, with the flow rate being equal to 0.75 mg/s, determined by the equivalent weight hourly space velocity (WHSV) used during the experimental investigation [52]. The flow is assumed to consist of air at atmospheric pressure and temperature. Fluent solves the mass and momentum conservation equations for the fluid phase in their steady-state and laminar form, as per Eqs. (1) and (2), respectively

[63]. The direction of the gravitational acceleration followed the flow path, i.e., from inlet to outlet.

$$\nabla \cdot \left(\rho_f \vec{v}_f\right) = 0 \tag{1}$$

$$\nabla \cdot \left(\rho_f \vec{v}_f \vec{v}_f\right) = -\nabla P + \nabla \cdot \bar{\bar{\tau}} + \rho_f \vec{g} \tag{2}$$

Here, $\vec{v}_f$ and ρ_f are the fluid velocity and density, respectively, P is the pressure drop, $\bar{\bar{\tau}}$ the stress tensor and $\vec{g}$ the gravitational acceleration. The SIMPLE algorithm was used for the pressure-velocity coupling, utilising a Second Order upwind scheme. Under-relaxation factors of 0.1 were used for pressure and momentum and of 0.5 for density and body force. The residual targets of $1e^{-3}$ and $1e^{-4}$ yielded very similar results, with an average error of 4% as per Table A10 of the ESI. Consequently, to allow for easier convergence and reduce the computational time necessary, the residuals target was set to $1e^{-3}$ during the comparison of the different test cases. Solution proceeded until convergence was reached. All cases were simulated on the IRIDIS 5 high performance computing facility, utilising 2 Intel Xeon 6130 2.1 GHz CPUs, with 32 Gb of allocated RAM. Computational resource utilisation is based on five metrics, mesh size, file size, iterations needed for convergence, simulation time, and RAM utilisation, as those are defined in our previous [64].

3. Results

3.1. Image-processing impact on bed structure

The impact of the different test cases on the bed structure is evaluated through the radial and axial porosity profiles, as well as through the bulk porosity. The un-processed section (TC-Original) is used as validation. The results in this section refer to the processed binary images before mesh generation. The radial, axial, and bulk porosity of the different test cases are presented in Fig. 3a-c, respectively. It is important to mention here that for the context of this work, the term "porosity" refers to the interparticle porosity of the fixed bed, i.e., the overall voidage. This corresponds to the fraction of the total volume of the empty space and of the total volume of the bed. A detailed comparison of the unprocessed and full 3D CT-scanned bed porosity with existing empirical correlations, determined for spherical beds, has been presented in our previous work [52].

Errors are cumulatively introduced in the final geometry, based on the number and the crudeness of the processing operations, causing the processed geometries to deviate from the original. Noticeably, the trends in the radial and axial porosity profiles are well captured from all test cases. Specifically, the radial location and the period of the various oscillations are both accurately reproduced. However, the amplitude of these oscillations is significantly increased as the CT-images are more heavily processed. With TC-0 (Erode-Dilate), changes in the radial and axial porosity profiles, Fig. 3a and b, respectively, are barely noticeable, especially in the near-wall section. Differences become more prominent only in the radial profiles close to the bed centre, at a radial length above 1.7. Specifically, initially, TC-0 presents higher porosity magnitudes in-between the radial lengths of 1.7–1.8, but past the 1.8 radial length it presents lower magnitudes, compared to TC-Original. Due to the very small area covered by the concentric rings at these regions, small processing modifications can have a seemingly bigger effect. The marginal error introduced by TC-0 is also demonstrated by its bulk porosity, Fig. 3c, which is increased by 0.6% compared to the original geometry. The radial and axial profiles between TC-1 and TC-2 are almost identical; both cases present

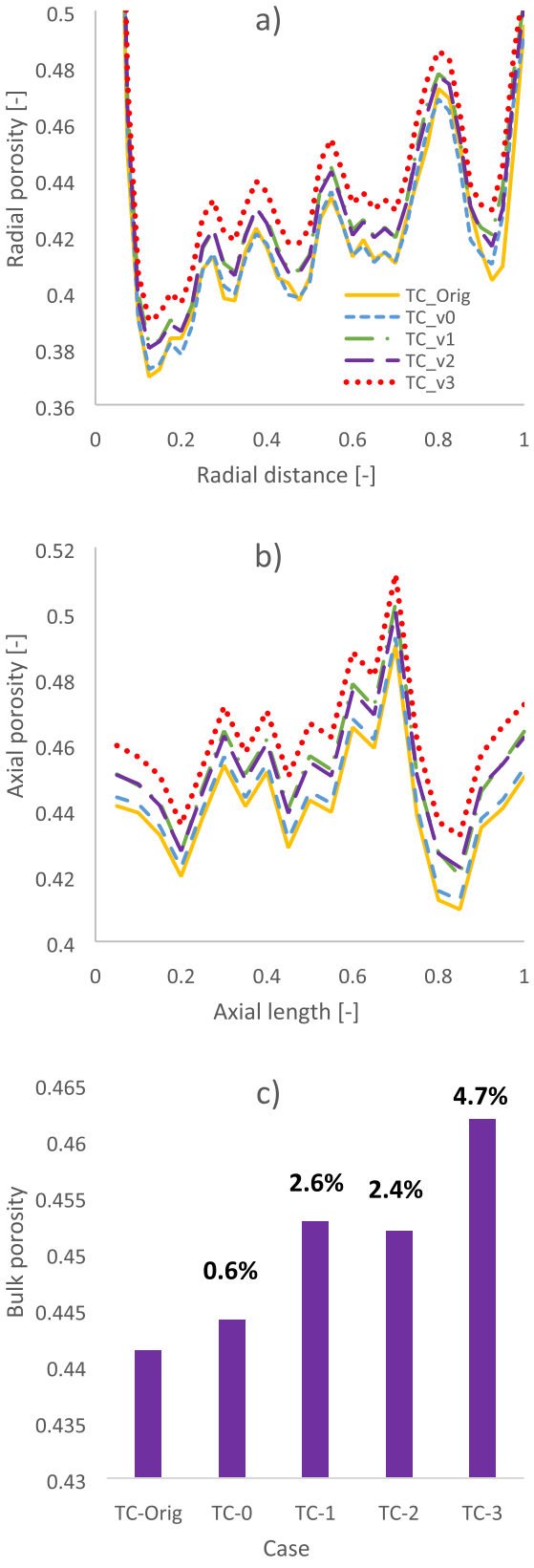

Fig. 3. A) Radial, b) axial, and c) bulk porosity of the 10% 300–500 μm section, as a result of the image-processing methodology.

radial and axial oscillations larger in magnitude compared to those of the original geometry, across the entire radial distance and axial length. Their error in terms of bulk porosity is also similar, equal to

2.6% and 2.4% for TC-1 and TC-2, respectively. Finally, the crude processing of TC-3 results in radial and axial profiles with significantly larger magnitudes compared to those of the original geometry. These differences are further highlighted by the large error in bulk porosity, which reaches 4.7%.

For all test cases, the increase in their porosity magnitude corresponds to a reduction in the particle volume. This is reasonable as the intended outcome was to remove dust particles. For TC-0, by initially shrinking the particles, the "Erode" operation removes dust particles consisting of few voxels, while the subsequent expansion, applied by the "Dilate" operation, returns the remaining particles to their original form. This combination results in marginal changes to the original geometry and very small errors, as indicated by the bulk porosity changes of TC-0. On the contrary, the"Fill holes" operation (TC-1) irreversibly deforms topological features by covering existing cavities, thus introducing a 2.6% error in the bulk porosity. While TC-1 fills interparticle cavities in particle clusters, i.e., increasing the particle volume and reducing porosity, it also removes volume from isolated particles. Consequently, TC-1 results in a net-negative catalyst volume, hence in a porosity increase. Instead, the "Close" operation (TC-2) is a gentler processing method, as, by essentially repeating the TC-0 process ("Dilate" then "Erode"), morphological structures are better preserved. Here however, with the original geometry having been already deformed after the application of TC-0, subsequent repetition further exacerbates topological errors by removing additional particle surface. This accumulates in a 2.4% error, compared to the original geometry. Consequently, no matter how delicate, each subsequent operation introduces permanent deformations, which accumulate into ever-increasing errors. This is highlighted by TC-3, where, by gradually repeating the "Erode" and "Dilate" operations, errors escalate to 4.7%. Despite the errors introduced by all processing operations, however, the trends in the radial and axial porosity profiles are well preserved. Thus, by inspecting the flow fields through these geometries, unique insights into the coupling between bed structure and hydrodynamic profile can be produced.

With the processing operations modifying the catalytic particles, changes to the interparticle network are inevitable. Consequently, with the hydraulic diameter, i.e., the size of the interparticle pores, being another key parameter for the permeability of the catalytic bed [65,66], the severity of these changes should be estimated. The normalised distributions of pore volume and of coordination number, for the various test cases, are presented in Fig. 4a and b, respectively. Distribution is normalised around the average value of the pore volume and of the coordination number metrics, respectively. Distribution reveals the population of pores sharing a similar magnitude of the considered metric. The comparative error of these metrics, with regards to the original geometry, is also presented next to each figure (unless that error is 0.0%). The total number of pores for the different test cases is presented in Figure A2 of the ESI.

TC-0 has an almost identical pore network compared to the original geometry. Specifically, both the pore number, Figure A2 in the ESI, and the pore volume distribution, Fig. 4a, are the same as TC-Original. Minor errors, around 0.1%, are only presented in the coordination number. TC-1 has the largest combined error compared to the original geometry, with an average absolute error of 21.1% and 24.3% in the pore volume and coordination number distributions, respectively. Specifically, here, the distribution of larger pores is increased whilst their connectivity is reduced. On the contrary, the distribution of smaller pores is reduced, but their connectivity is increased, compared to the original geometry. Furthermore, the total number of pores is reduced by 4.4%, as per Figure A2. Similar conclusions can be reached for TC-3, however here, the effect is not as invasive. The shift in the distribution of larger pores is slightly larger for TC-3 than for TC-2, compared to TC-Original, equal to 22.6%, but the error in the network connectivity and in the total number of pores is now reduced to 13.6% and 3.0%, respectively. On the contrary, TC-2 preserves the interparticle pore network better, reducing the errors in the pore volume and coordination number distributions to 10.6% and 5.8%, respectively, and the error in the total number of pores to 0.3%. These three test cases, TC-1, -2, and -3, introduce similar changes to the interparticle network, albeit with a different error intensity. By interpreting the results, it can be understood that, by deforming the catalytic particles and the cavities they form, image-processing merges neighbouring pores together, forming a simpler, less interconnected network.

3.2. Mesh characteristics

As discussed in the introduction, meshing narrow topological features and treating contact regions without introducing significant errors in the final geometry is an important consideration in the CFD literature. Consequently, with Simpleware segmenting the particles to deal with contact regions, it is important to confirm that the local bed structure, in terms of radial, axial, and bulk porosities, is preserved. For this purpose, the pre- and post-meshing radial and axial porosity profiles are presented in Figure A3-A7 of the ESI for all test cases, while the bulk porosity of the different test cases is presented in Fig. 4. In addition, the mesh and file size of the different test cases are presented in Table 3, while their mesh quality metrics are all presented in Figure A8-A9 of the ESI.

For all test cases, their post-meshing radial, axial, and bulk porosity magnitudes are higher compared to their pre-meshing values. This signifies that, by segmenting the particles from their neighbours, Simpleware removes particle regions, thus further reducing the overall bed volume. Meshing introduces the highest error in the original, unprocessed, test case, TC-Original, where a volume difference of 0.9% between its pre- and post-meshing bulk porosity, Fig. 4, is observed. As the original test case was unprocessed, the dust particles were retained. However, meshing removed those regardless, hence the difference in the bulk porosity. Consequently, the bulk porosity of the original test case reached a magnitude equivalent to that of the post-meshed TC-0. This confirms that meshing the original CT-geometries without any topological changes is not possible, and that deformations are inevitable. For all other test cases which had already underwent processing prior to meshing operations, their post-meshing bulk porosity presents a very small increase of 0.2%. An error of this magnitude enforced by meshing operations is acceptable and reasonable [48], considerably smaller than the 1.7% error reported by Wehinger *et al.* [18] and the 1.38% error reported by Partopour and Dixon [21] during meshing of their mono-dispersed cylindrical beds using the "caps" and the "bridges" method, respectively. Moreover, the radial and axial porosity profiles are accurately resolved during meshing, as per Figures A3-A7 of the ESI, retaining the oscillations trends with a reasonable accuracy, albeit with a slightly larger porosity magnitude, as already discussed. This is a testament to the capability of Simpleware in preserving complex topological features, even in its coarsest settings.

Regarding the mesh statistics of the different test cases, presented in Table 3, with their geometry now being very similar in terms of porosity, TC-Original and TC-1 have comparable mesh and file sizes. Specifically, their computational mesh consists of 16 million cells and the resulting file size is equal to 1.5 Gb. This is a considerable mesh and file size, making loading, resolving, and processing of the test cases significantly more demanding compared to the remaining test cases. Their considerable mesh

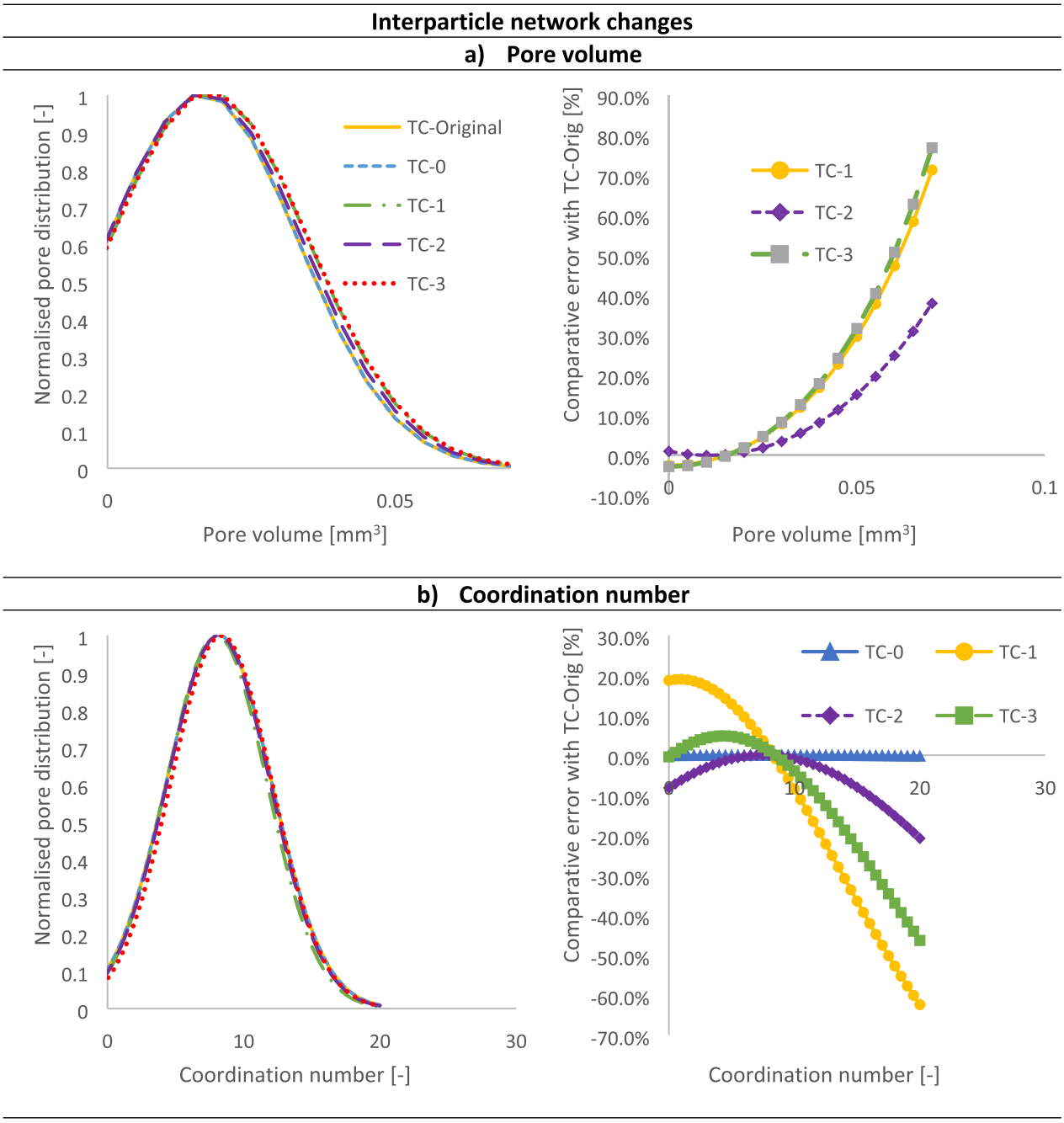

Fig. 4. Normalised distribution of a) pore volume and b) coordination number of the interparticle network, as a result of different image-processing methods. The comparative error of these metrics, with regards to the original geometry, is also presented (unless this error is 0.0%).

and file size originates from the volume of their computational cells, which are on average much smaller compared to the remaining cases, equal to $3e^{-15}$ m^3 as per Figure A8d of the ESI. With these cases preserving the most complex topological features, however, the necessity for a much smaller element size is justified. Both the mesh and the file size are significantly reduced with TC-1 and TC-2, now being equal to 12 M/1.2 Gb and 11 M/1 Gb as per Table 3, respectively. These cases also have the largest computational cell volumes, equal to $4e^{-15}$ and $4.5e^{-15}$ m^3 for TC-1 and TC-2 as per Figure A8d of the ESI, respectively. The similarities in the mesh statistics between TC-1 and TC-2 are reasonable, as both cases apply comparable changes to the geometry in terms of porosity and interparticle network. It is interesting to notice though that TC-2, apart from more accurately preserving the bed structure compared to TC-1, also achieves the largest reduction, ≈32%, in both the mesh and the file size. Consequently, the deformations introduced by the "Fill holes" operation in TC-1 are more difficult

Table 3
Mesh size and file size of the different test cases.

	Mesh statistics	
	Mesh size [–]	**File size [Gb]**
TC-Original	16.1 M	1.53
TC-0	16.2 M	1.54
TC-1	12.3 M	1.17
TC-2	11.0 M	1.04
TC-3	15.0 M	1.37

to mesh and to resolve, thus requiring 1 million additional cells. Finally, the mesh and the file sizes of TC-3 are comparable to those of TC-Original and TC-0, albeit slightly smaller. Its computational element volume is also comparable to them, being equal to $3.3e^{-15}$ m^{-3} as per Figure A8d of the ESI. Overall, Simpleware was capable of detecting narrow regions within the porous medium and utilised the smallest cell volume there. Specifically, for all test cases, more than 95% of the total cell population had a cell volume below $1e^{-14}$ m^3, and cells with larger volumes only appeared in the free flow regions. This resulted in such narrow regions having a sufficient number of cell layers in-between them, i.e., $\geq$5, allowing for accurate flow resolution.

Noticeably, the mesh quality of almost all cases is almost identical, as indicated by the orthogonal quality, the skewness, and the aspect ratio of the computational cells, shown in Figure A8a-c of the ESI, respectively. TC-Original and TC-0 display the best mesh qualities, due to their much smaller cell volume. Compared to them, TC-1 and TC-2 have a roughly 1% increase in the population of computational cells with medium (i.e., 0.3–0.7) orthogonal qualities, at the expense of the population with higher (i.e., >0.7) orthogonal qualities, as per Figure A9a of the ESI. Simultaneously, a similar 1% increase in the population of cells with medium (i.e., 0.3–0.7) skewness at the expense of the population with lower skewness (i.e., >0.3) is also observed in Figure A9b of the ESI. On the contrary, TC-3 has a considerable reduction in its mesh quality, consisting of cells with much lower orthogonal qualities and much higher skewness and aspect ratios, as indicated by both Figures A8-A9 of the ESI. The crudeness of the image-processing in TC-3, apart from significantly altering the bed structure, also creates an inter-particle network with harder to mesh topological features, forcing deformed computational cells of pour quality.

3.3. Flow velocity

Prior to comparing the different cases, it is key to understand the hydrodynamic behaviour of the reactor. To reveal the interconnection between velocity and porosity, Fig. 6a and b show the radial and axial Z-velocity profiles for TC-Original, respectively, in relation to the respective radial and axial porosity profiles. Radial and axial Z-velocity contour plots are also presented. The radial contour plot showcases the same 2D slice as Fig. 1, while the axial contour plot rests at the middle of the bed. Respective X- and Y-velocity plots are presented in Fig. A10-11 of the ESI.

By comparing the X-, Y-, and Z-velocities, the Z-velocity magnitude is around 1 to 2 orders of magnitude higher than the X- and Y-velocities, thus the primary flow path is from inlet to outlet, through the porous medium. However, X- and Y- velocities still exist, revealing that flow disperses in all directions, thus exhibiting distinct 3D behaviours. Consequently, with Z-velocity being the primary flow path, it is further analysed here. For the radial profile, Fig. 6a, the impact of the bed structure on the flow velocity is clear, with the Z-velocity presenting the same oscillation peaks as that of porosity. This is confirmed by observing the respective contour plot; the magnitude of Z-velocity remains similar along the same concentric radial slices, presenting peaks in the pores near the wall region and in the pores close to the bed centre. However, along the axial length, Fig. 6b, the interconnection between the two parameters appears random. The highly heterogeneous nature of the flow velocity within the porous medium is evident by inspecting the respective contour plot. Specifically, as a result of the local inter-particle network, referring to the interconnection of a pore with its neighbours in all three spatial dimensions, some pores exhibit significantly larger velocity magnitudes compared to their neighbours. It is also worth mentioning that minor flow recirculation within individual pores was also observed, as is evident by the negative magnitudes of Z-velocity. However, such recirculations were minor compared to the overall flow rate. Moreover, as indicated by the radial porosity of the bed, porosity is increased in the central bed region, thus leading to higher local Z-velocity magnitudes. This is indicative of the existence of a channelling effect, i.e., region of low packing density where flow moves through uninterrupted, which usually takes place only in the near-wall section [42,67]. This is especially evident in the contour plot of Fig. 7b, where a path of high flow velocity magnitude exists in the exact centre of the bed. In the literature, it has been reported that local velocity can be significantly higher than the superficial velocity of the bed [17,29,68]. The results here agree with this observation, with the maximum Z-velocity magnitude exhibited by the flow in TC-Original being 16-times higher than the average superficial Z-velocity magnitude. Moreover, it can be observed from the two contour plots of Fig. 6 that some particles reside in regions of low velocity magnitudes. This raises questions regarding the heat transfer capabilities of the bed, the accessibility of these particles to the reactants, and whether these particles are chemically inactive. This will be investigated in our subsequent study, where heat transfer and intraparticle physicochemical phenomena will be introduced. It will also be very informative to compare the intra-particle physicochemical phenomena of our poly-dispersed bed with those produced from homogeneous spherical and/or cylindrical particles. This comparison will further highlight their differences and increase our understanding regarding the impact of poly-dispersity. This would be highly valuable even for industrial applications that utilise perfect particle shapes, as these particles could potentially fracture, degrade, or deform over time, especially considering their harsh operating environments. In such cases, it is key to understand how complex particle shapes could affect the local transport phenomena. Moreover, characterising the association between turbulence and poly-dispersity will also be key for industrial applications, as they predominantly utilise high flow rates for increased productivity.

The normalised Z-velocity magnitude distribution, as well as the radial and axial Z-velocity magnitude profiles, for all test cases are presented in Fig. 7a-c, respectively. In Fig. 7a, Z-velocity distribution, i.e., the Z-velocity within each computational cell within the porous medium, is normalised around the average Z-velocity magnitude of each test case, with the standard deviation being used to define the Gaussian distribution curve. The radial and axial Z-velocity magnitude profiles are defined in the same concentric rings used to evaluate the radial and axial porosity profiles of Fig. 3a and b, respectively. Radial and axial plots for the X- and Y-velocities of all test cases are presented in Figures A12-A13 of the ESI, respectively.

The Z-velocity distribution, radial Z-velocity, and axial Z-velocity profiles are roughly identical in-between TC-Original and TC-0, as per Fig. 7a-c, respectively, further highlighting their resemblance in terms of pre- and post-meshing bed structure. On the contrary, for Z-velocity distribution, Fig. 7a, the remaining TCs show a shift of the average velocity magnitude towards higher values. Specifically, compared to TC-Original, TC-1 shows an increase of 10.5% and 5.8% in its average Z-velocity magnitude and standard deviation, respectively. Instead, while TC-2 presents a larger average Z-velocity magnitude, increased by 15.5%, its standard deviation is closer to that of TC-Original, with an error of 1.4%. Finally, for TC-3, its average Z-velocity magnitude is increased by 21.9%, while its standard deviation is smaller than that of TC-Original by 2.1%.

Rationalising these results, it can be understood that flow through the medium is now faster for TC-1, -2, and -3, with TC-1 and -2 also showcasing a wider range of velocities compared to TC-Original and TC-3 showcasing a narrower range. Interestingly, these results reveal an interconnection between the pore structure and the flow velocity. By normalising Z-velocity, pore number, pore

volume, and coordination number of the different test cases against those of TC-Original (excluding TC-0 due to resemblance) and plotting them on the same figure, Figure A15 of the ESI, some trends can be observed. Specifically, for all three TCs, pore number and pore volume do not seem to have a clear association with the flow velocity. On the contrary, as coordination number increases from 8.0 (TC-1) to 8.2 (TC-2) and to 8.4 (TC-3), a clear linear relationship with Z-velocity magnitude can be observed. These results indicate that coordination number has a higher impact on the flow velocity compared to the pore number or the pore volume. However, this necessitates a dedicated parametric study to fully comprehend the association between the bed structural parameters and the bed's hydrodynamic behaviour, thus pinpointing the primary driving factors.

The radial and axial Z-velocity profiles, Fig. 7b and c, respectively, as well as the radial and axial profiles of X- and Y-velocities, Figures A12 and A13, respectively, also showcase the sensitivity of the flow velocity to minor changes in the local topological structure. As previously discussed, TC-2 presented porosity, Fig. 3, and interparticle network characteristics, Fig. 4, closer to those of TC-Original, compared to TC-1. As a result, TC-1 presents the largest errors in its X- and Y- radial and axial velocities when compared to TC-Original, as per Figures A12 and A13, errors which are even larger than those of TC-3. Specifically, while the radial and axial X- and Y-velocity profiles of TC-1 follow the overall trends of TC-Original, due to minor changes in local topological features, its X- and Y- velocity magnitudes are considerably different. However, the radial and axial Z-velocity magnitude profiles, Fig. 7b and c, respectively, show a different behaviour. Specifically, for the radial Z-velocity in-between the radial distance of 0.3 to 1.4 mm from the wall, TC-2 presents overall higher Z-velocity magnitudes compared to TC-1. Furthermore, TC-2 presents overall higher Z-velocity magnitudes along the entire axial length, compared to TC-1. Consequently, the radial and axial Z-velocity profiles predicted by TC-1 are closer to those of TC-Original than the profiles predicted by TC-2. Finally, while TC-3 was the crudest image-processing method in terms of preserving the porosity and interparticle characteristics, its X- and Y-velocity profiles are closer to TC-Original than those of TC-1, albeit slightly, but its Z-velocity profiles present the largest overall errors out of all other test cases. The conflicting observations of the X-, Y-, and Z-velocity profiles between TC-1 and TC-2 showcase that minor topological differences in the pore structure, which are not easily detectable by simply observing the 2D radial and axial profiles of porosity and interparticle network, can result in considerable differences in the flow velocity. To accurately interpret these results, a truly holistic analysis is required, exploring the association between the 3D bed structure and the local flow velocity. As also highlighted by Partopour and Dixon [8], the 3D visualisation and interpretation is a field which can greatly benefit by machine learning.

3.4. Flow static pressure

Prior to examining the different cases, the radial and axial static pressure profiles of TC-Original are presented in Fig. 8a and b, respectively. In addition, respective contour plots are also presented. The negative pressure values appearing in the contour plot of Fig. 8b are the result of minor backflow at the outlet of the reactor. It can be seen in both the scatter plot and the contour plot of Fig. 8a that, radially, static pressure presents random oscillations with no discernible pattern. As a result, neighbouring pores with significant pressure gradients can exist. Furthermore, by comparing the Z-velocity contour plot of Fig. 7a with the pressure contour plot of Fig. 8a, it can be seen that local regions of accelerated Z-velocity result in local pressure minima, however, the X- and Y-velocities also play a role in the resulting pressure drops, further supporting the complex role of local 3D topological features. Pressure is lower near the centre of the bed, in the region where the channelling effect is observed, and the flow field accelerates. Along the axial length, Fig. 8b, static pressure presents a linear drop of around 17 Pa.

Fig. 9a and b present the radial and axial pressure drop profiles of the different TCs. As expected, TC-Original and TC-0 have very similar pressure drop profiles, along both the radial and axial directions. Along the axial static pressure profile, the average absolute error of TC-0, compared to TC-Original, was 0.45%. For TC-1, following its Z-velocity trends, its axial pressure drop is the closest to that of TC-Original out of the remaining test cases, with an average absolute error of 1.4%. Interestingly, however, its radial pressure drop profile is the highest out of all five test cases, thus showcasing the importance of accurately resolving the X- and Y-velocity profiles as well. The remaining two cases, TC-2 and TC-3, both have lower radial and axial pressure drop profiles compared to TC-Original, with TC-2 exhibiting the lowest magnitudes. As a result, TC-2 has the largest error in its axial pressure drop, compared to TC-Original, equal to 9.8%, while the respective error of TC-3 is equal to 6.6%. An important thing to notice in Fig. 9a is that the sudden pressure drop in the central bed region due to the channelling effect exists only for TC-Original and TC-0. All other test cases present smaller local pressure gradients. This is indicative of the sensitivity of pressure drop to the local bed structure, as small changes in the topological features in this region due to image-processing significantly modifies the resulting velocity, Fig. 7b, and pressure, Fig. 9a, fields.

Literature studies that focused on the impact of the bed structure on the pressure drop insisted on preserving the catalytic bed structure, in terms of bulk and radial porosity, as much as possible [17,18,30,48]. In fact, Dixon *et al.* suggested as a rule of thumb that a 1% change in the bed's porosity leads to a 3% change in the pressure drop [48]. Here, in the first two sections, it was determined that, in-between TC-1, -2, and -3, TC-2 was the most delicate processing method, respecting the bed structure the best, both in terms of bulk, radial, and axial porosities and in terms of interparticle network. However, the deviations in its Z-velocity and static pressure parameters were larger than those of TC-1, and in the case of pressure drop, even larger than TC-3. With both TC-1 and TC-3 methods being more invasive in their processing, this is an unexpected result. Summarising the bulk porosity and the static pressure results, compared to TC-Original, the errors in the bulk porosity were equal to 0% (TC-0), 2.0% (TC-1), 1.7% (TC-2), and 4.0% (TC-3), while the errors in the axial pressure drop were 0.5% (TC-0), 1.4% (TC-1), 9.8% (TC-2), and 6.6% (TC-3). This means that a 1% change in the bed's porosity leads to a 0.7% (TC-1), 5.8% (TC-2), or 1.7% (TC-3) change in the pressure drop. Consequently, due to the highly complex and poly-dispersed nature of the considered beds, it is not easy to identify a straightforward connection between porosity and pressure as the one suggested by Dixon *et al.* [48], and doing so neglects key parameters that play a dominant role. It is thus clear that there is a complex and delicate interplay between structural morphology (i.e., porosity and pore distribution) and hydrodynamic profile (i.e., velocity and pressure drop), where minor changes in the structural system cause considerable results in the flow field. Fully understanding the interplay between local bed porosity, pore size and connectivity, and flow profiles, dedicated computational studies are needed, where the impact of these parameters can be investigated dynamically.

3.5. Computational resources

The computational resources of the different test cases are presented in Table 4, evaluated based on the number of iterations and computational time needed for convergence, as well as on RAM

Table 4
Computational resources of the different test cases. Simulations were performed on IRIDIS 5 high performance computing facility, utilising 2 Intel Xeon 6130 2.1 GHz CPUs, with 32 Gb of allocated RAM.

	Computational resources		
	Iterations[–]	**Computational time [min]**	**RAM Utilisation [Gb]**
TC-Original	251	27	28
TC-0	243 (−3.2%)	26 (−3.7%)	28.1 (0.5%)
TC-1	230 (−8.4%)	19 (−29.6%)	22.2 (−20.7%)
TC-2	231 (−8.0%)	16 (−40.7%)	20.5 (−26.7%)
TC-3	266 (6.0%)	24 (−11.1%)	26.3 (−6.0%)

utilisation. The parenthesis next to each metric showcases its difference with the respective metric of TC-Original.

The resemblance between TC-Original and TC-0 continues, as the computational resources of the two cases are very close together. However, TC-0 is comparatively cheaper, reducing the computational time and number of iterations needed by around 3%-4%. In terms of hardware requirements, i.e., file size (Table 3) and RAM utilisation (Table 4), the two cases are very close, with TC-0 being slightly more expensive. Comparatively, TC-2 is the fastest case explored, requiring 16 min to complete 231 iterations, reduced by 41% compared to TC-Original. Furthermore, TC-2 has the smallest hardware requirements, both in terms of file size (Table 3) and RAM utilisation (Table 4), with a reduction of 32% and 27%, respectively. TC-1 is slightly more expensive compared to TC-2, requiring 19 min for 230 iterations, reduced by 30% compared to TC-Original. Its hardware requirements are also reduced by 24% (file size) and 21% (RAM utilisation), but the achieved reduction is not as large as that of TC-2. Finally, the computational demands of TC-3 are slightly cheaper compared to TC-Original, with a reduction of 11% in the computational time, requiring 24 min to achieve 266 iterations. Its reduction in the hardware requirements is also small, equal to 10% (file size) and 6% (RAM utilisation).

While the computational demands presented here may seem low, the reader is reminded that only a 10% section of the full bed was studied. Furthermore, simply the laminar flow or air through the medium was considered, thus solving only the mass and the momentum conservation equations. In the future, we are looking to expand these simulations to include heat transfer, as well as diffusion and reaction phenomena. To validate with available experimental results, the bed should also be scaled-up to a 50% section. With those modifications in mind, keeping the computational demands manageable is critical. In our previous work, we highlighted the dilemma faced by computational engineers, specifically the need to preserve computational accuracy while reducing simplifications and errors [53]. Furthermore, it was previously discussed that, even if the CT-scans are left unprocessed, geometry modifications during meshing are inevitable, thus errors will always be introduced. If the goal is to investigate the hydrodynamic behaviour of the bed as accurately as possible, then the methods followed by TC-Original or TC-0 are advised, as their topological structures and flow profiles are practically identical. If the goal is to scale-up, introduce heat transfer, and solve for physicochemical phenomena (diffusion and reaction), then the method followed by TC-2 is advised. This method introduces relatively small errors in the bed structure, i.e., 1.8% error in the bulk porosity post meshing and compared to TC-Original, as per Fig. 5c. However, its errors in the velocity and pressure profiles were significant, ≥10%. But the reduction in the computational resources achieved cannot be understated. With the pressing need to explore and understand all aspects of fixed bed chemical reactors during operation, especially for poly-dispered beds where both catalytic and experimental data are scarce, TC-2 is the best candidate for further investigations.

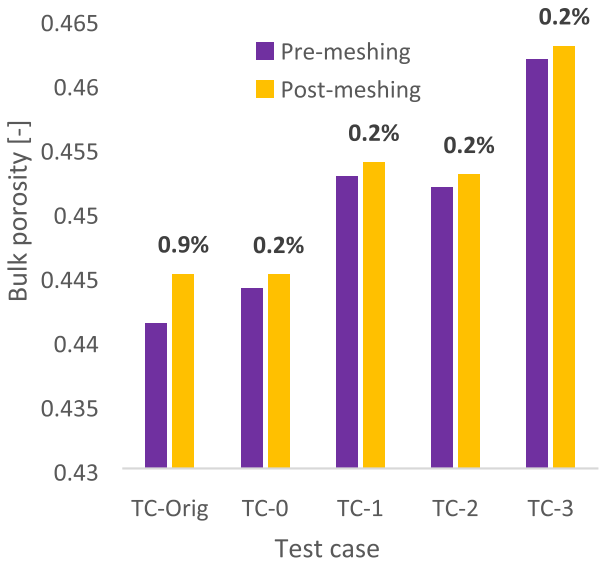

Fig. 5. Bulk porosity of the different test cases, before and after the geometry was meshed.

3.6. Particle size study: Hydrodynamics of 300–500 μm and 500–700 μm beds

The poly-dispersity of the particles within the bed structure was seen to play a prominent role in the flow profiles. However, identifying the role of the particle size in these flow profiles is highly valuable for optimising the reactor's performance. For this purpose, the 10% section of the 300–500 μm bed is compared with the respective 10% section of the 500–700 μm bed. Both beds were processed using the TC-2 method. Furthermore, for these simulations, the residual targets were reduced to $1e^{-4}$ from $1e^{-3}$, leading to higher solution accuracy. The computational resources of the two cases are presented in the Table A1 of the ESI. The radial and bulk porosity, as well as the pore size distribution and total pore number, of the 300–500 and 500–700 μm cases are presented in Fig. 10a and b, respectively. Both metrics of Fig. 10 refer to the 300–500 and 500–700 μm cases after they have been processed with the TC-2 method and meshed. The axial porosity and coordination number of the two cases is presented in Figure A16 of the ESI.

Due to its smaller particle sizes, the 300–500 μm bed presents a more heavily packed structure and a more complex pore network. Comparatively, the 500–700 μm bed presents very large radial porosity oscillations along the entire radial length of the bed, while its overall bulk porosity is 3% larger, signifying a less tightly packed bed. Furthermore, as was discussed in our previous work, the 10% section of the 500–700 μm bed has a highly heterogeneous structure [53], because of its larger particle sizes. Consequently, with its larger particles being deposited at various orientations, the interparticle pores formed are fewer in number and much larger in volume compared to those formed by the 300–500 μm bed. However, the coordination number of the interparticle network is similar between the two cases, as per Figure A16b of the ESI, with the 500–700 μm pores having a slightly smaller coordination number, i.e., less interconnected pores.

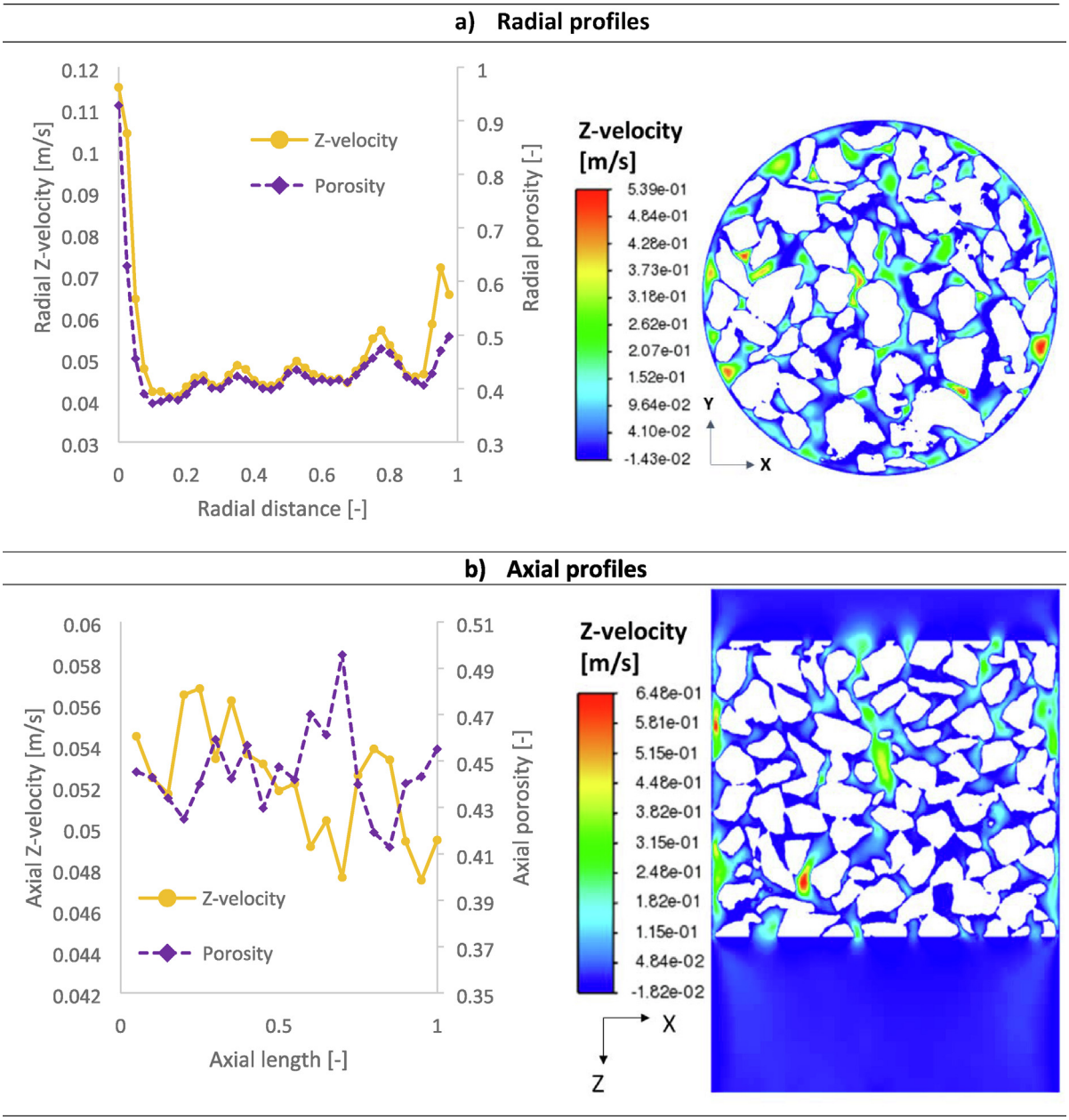

Fig. 6. A) Radial and b) axial z-velocity and porosity profiles of tc-original. in addition, radial and axial contour plots of z-velocity are presented.

The normalised Z-velocity distribution and radial Z-velocity profile of the 300–500 and 500–700 μm cases are presented in Fig. 11a and b, respectively. The radial and axial X- and Y-velocity profiles, as well as the axial Z-velocity profile, are presented in Figures A16-A18 of the ESI, respectively. Respective contour plots are presented in Figures A19-A24 of the ESI.

Although the radial Z-velocity profiles of the two cases are very similar, the 500–700 μm case presents overall lower magnitudes. Specifically, the average Z-velocity magnitude within the 500–700 μm bed is 2.9% lower compared to that within the 300–500 μm bed, being at a similar magnitude to the difference in the bulk porosity observed between the two cases. Both beds exhibit a highly heterogeneous flow field, with the maximum Z-velocity magnitude being 16-times and 14-times higher than the average Z-velocity magnitude in the 300–500 and 500–700 μm case, respectively. Comparing the radial Z-velocity profiles of the two cases from Fig. 11b, the 500–700 μm case presents higher Z-velocity magnitudes only in the near-wall section and at a radial depth of around 0.85 mm from the wall. The former is due to the near-wall channelling effect being more prominent as the particle size increases, while the latter is caused by the local peak in the radial porosity of the 500–700 μm case, observed in Fig. 10a. The 300–500 μm case has a stronger channelling effect in the central bed region, at a radial depth $\geq$ 1.8 mm from the wall, where, as a result of the local porosity increase, demonstrated in Fig. 10a, the local Z-velocity is considerably larger than that of the 500–700 μm case. The same conclusions can be reached by observing the contour plots of Figure A24-A25. With both porosity and pore volumes being smaller in the 300–500 μm bed, the flow faces more obstructions in its path. Due to the smaller pore sizes of the 300–500 μm bed, the flow is forced through narrower regions, compared to the flow in the 500–700 μm bed, thus it is locally accelerated reaching higher magnitudes. The flow velocity is directly associated with the permeability of the beds and with

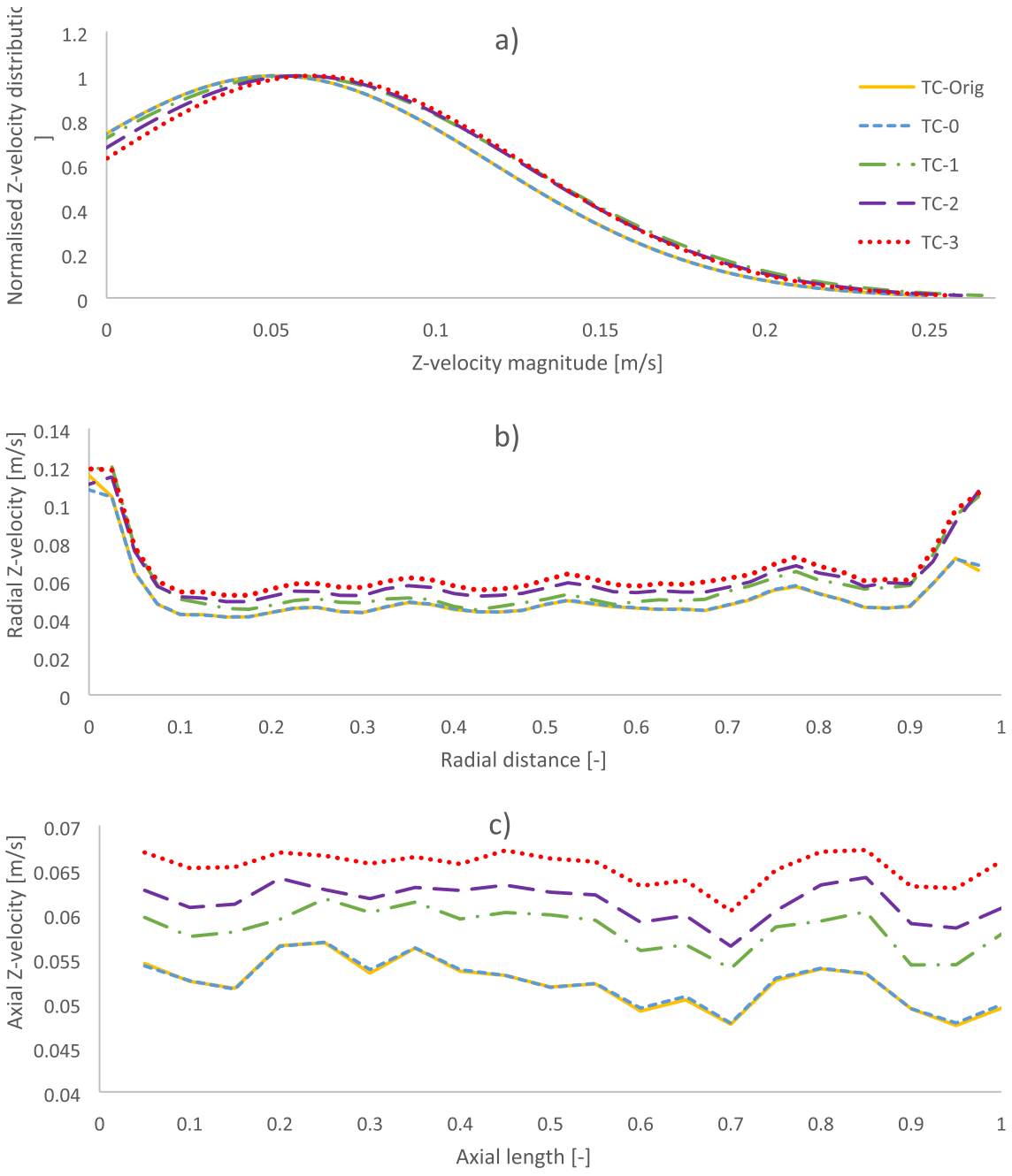

Fig. 7. A) z-velocity distribution, and b) radial, and c) axial z-velocity profiles for the different test cases.

the resulting pressure drop. To quantify this, the axial pressure drop of the two cases is presented in Fig. 12. Radial and axial static pressure contour plots are presented in Figures A25-A26 of the ESI, respectively. Increasing the particle size significantly reduces the pressure drop experienced by the bed. Specifically, the 500–700 μm case achieves a 52% reduction in its pressure drop compared to the 300–500 μm case.

Reducing the pressure drop of the catalytic bed is a key performance optimisation goal. Large pressure drops are not desirable, as they detrimentally increase the compressor power requirements, used to dictate the flow, thus hindering the efficiency of the system and increasing the costs [9,69]. The reduction of the pressure drop as the particle size increases is a well-known effect [15,70] which is also confirmed by our observations. However, reducing pressure drop is one aspect of reactor optimisation, with heat management and chemical performance being equality important. Heat management refers to the ability of the reactor system to rapidly remove heat produced from exothermic reactions, thus preventing local hotspots leading to catalyst sintering or runaway conditions [9,71]. Larger particles are known to exhibit lower temperatures, whilst they also form less heavily packed beds, thus allowing more effective and rapid heat removal through convection [9,15]. Chemical performance refers to the product yield of the chemical reactor. Aside from the operating conditions, e.g., flow rate, pressure, and temperature, intraparticle physicochemical phenomena, i.e., diffusion transfer, particle accessibility, and exposed surface area, also affect the overall reaction rate. Specifically, larger particles introduce intraparticle diffusion limitations that act as a rate-

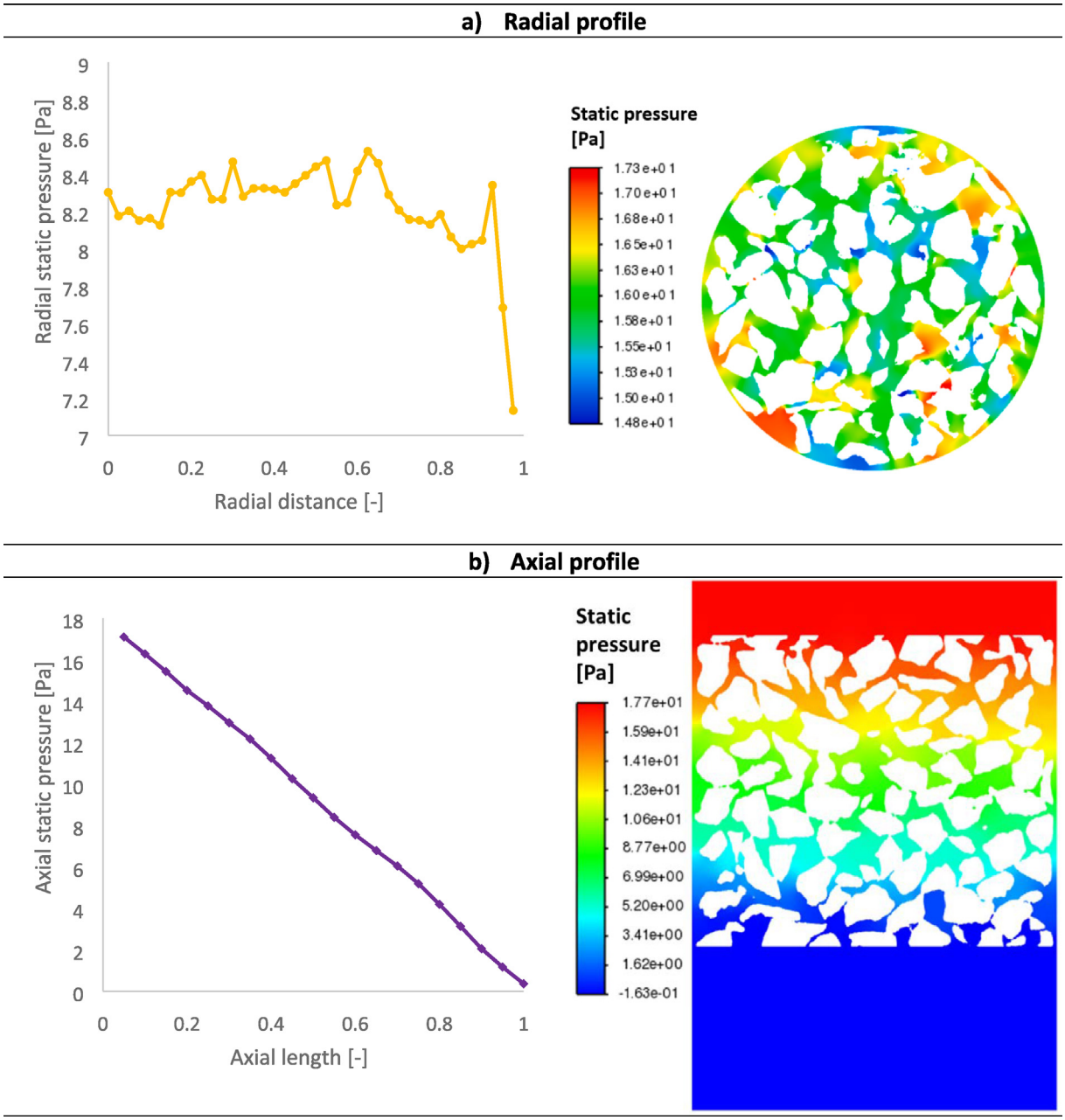

Fig. 8. A) Radial and b) axial static pressure profiles of tc-original. in addition, radial and axial contour plots of pressure are presented.

limiting step, while their exposed surface area is reduced compared to smaller particles, effects which both limit the performance of the reactor [15,72]. Consequently, reactor optimisation involves a delicate balance between these aspects. While the heat transfer and the chemical performance of the beds will be studied in our subsequent work, the exposed surface area and the species residence time within the bed can be investigated with our available cases.

The exposed surface area and the residence time of the 300–500 and 500–700 μm cases are presented in Table 5. For the calculation of the residence time, 18 k massless particles were injected within the porous medium every 10 iterations, and their position was tracked. Massless particles have no associated physical properties and experience no force; thus they don't interact with the flow, but rather move along the flow path [61]. The 300–500 μm case has a 30% higher surface area exposed to the flow, compared to the 500–700 μm case, thus allowing easier catalyst access to the reactants. However, despite its less complex interparticle network, the 500–700 μm case exhibits a slightly larger residence time, as a result of its lower overall flow velocities. Higher residence time is associated with more contact time between reactants and catalyst, thus increasing the possibility of reactants to chemically transform. It is unlikely that the small increase in residence time achieved by the 500–700 μm case will counterbalance the increase in the exposed surface area achieved by utilising the smaller catalytic particles. Further investigating the chemical performance of these case will enable a deeper understanding of how the different flow parameters are interconnected. This study will also reveal how particles residing in regions of low flow velocity behave.

The results seen here reveal interactions between the flow and the interparticle network that are not widely understood yet. Throughout the literature, porosity is the primary parameter to

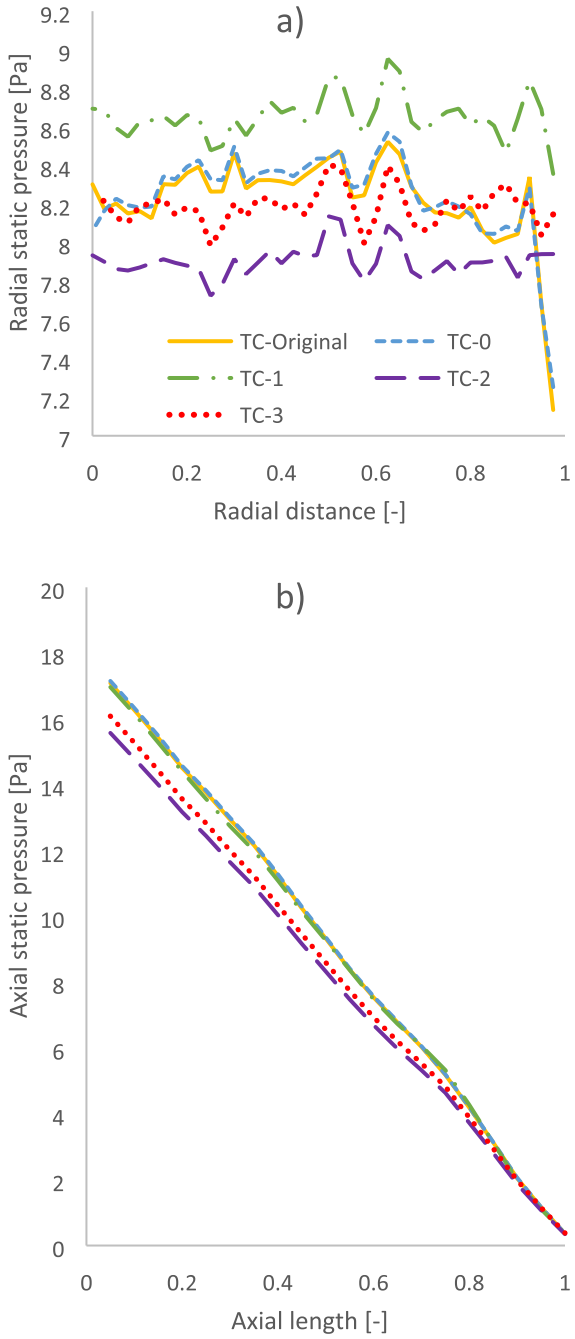

Fig. 9. A) Radial and b) axial static pressure profiles of the different test cases.

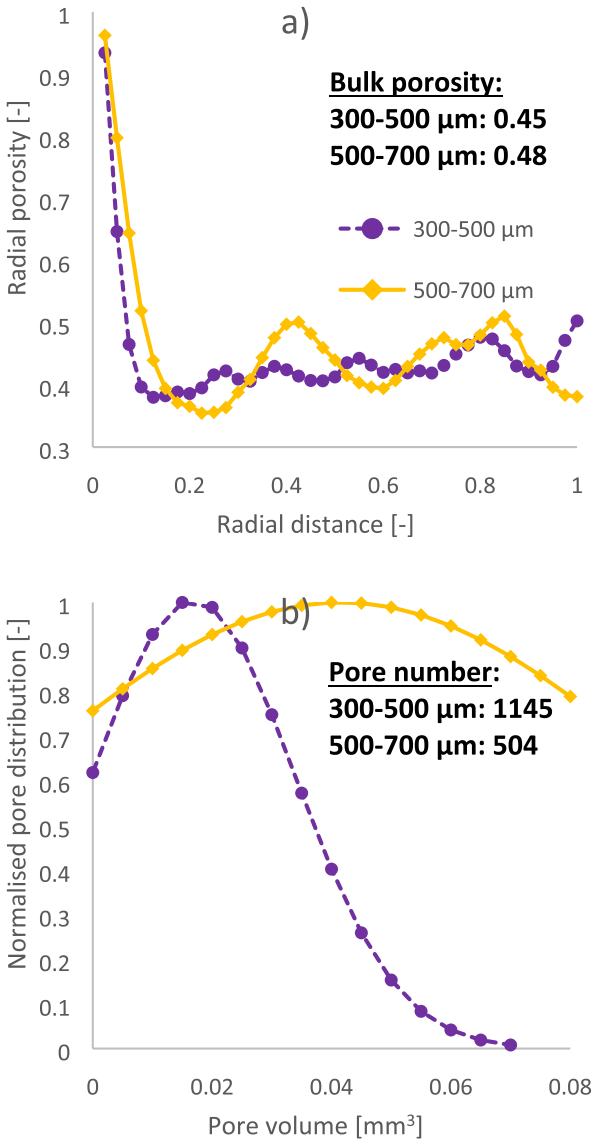

Fig. 10. A) Radial porosity profile and b) normalised pore distribution of the 10% sections of the 300–500 and 500–700 µm beds.

describe the bed structure, thus trying to preserve it during meshing as accurately as possible is of paramount importance. However, it was seen here that the interparticle network, and specifically the coordination number, can play an equally important role, especially regarding its 3D interconnectivity. The unique insights produced by the highly poly-dispersed beds considered here are key to advance our understanding regarding the hydrodynamic behaviour of fixed bed chemical reactors. However, for this, advanced methods to depict and interpret the results are necessary. Incorporating the heat transfer and the chemical reactions in the considered cases will further reveal how poly-dispersity affects the performance of the reactor, guiding future optimisation studies and accelerating the scale-up efforts towards our emission reduction goals.

4. Conclusions

Scaling-up and optimising fixed bed chemical reactors used for the bulk production of carbon-neutral fuels and chemicals requires the development of advanced Computational Fluid Dynamics (CFD) models. For this, coupling CFD models with experimental setups can provide unique insights into the behaviour of fixed bed reactors during operation. This becomes possible through the application of computed tomography (CT) scans, which produce a 3D representation of the internal structure of lab-scale reactors. Previously, such CT scans were used in our lab-scale fixed bed reactor, revealing its poly-dispersed nature, with particles exhibiting a wide range of sizes, shapes, and orientations. Here, a 10% section of these beds was used as a 3D geometry for CFD simulations. Prior to integrating the geometry, however, image-processing was applied to reduce the mesh size and the computational resources necessary. Based on the number of processing steps involved in

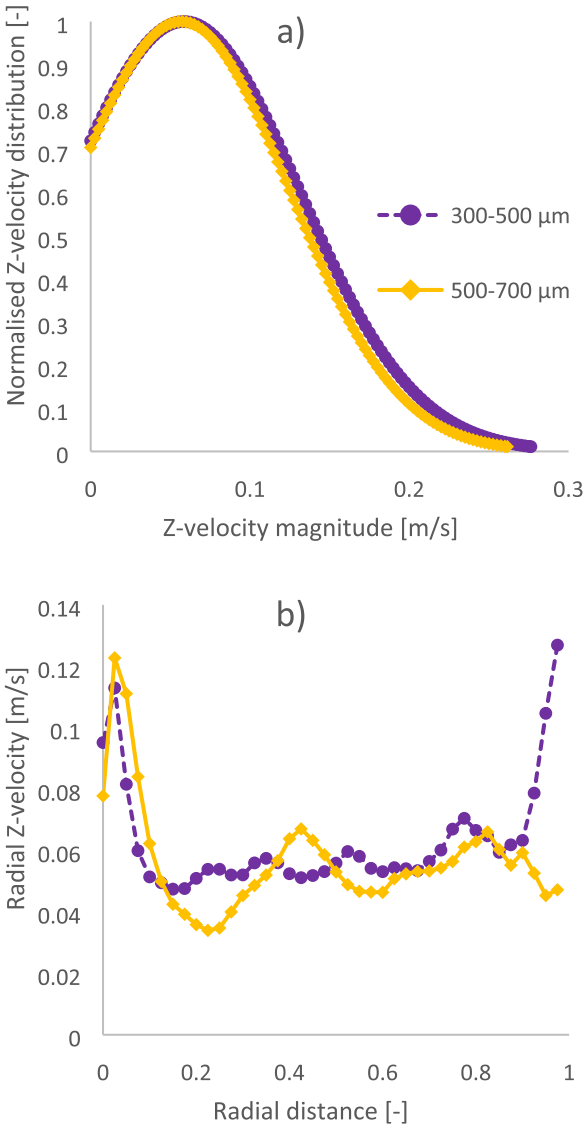

Fig. 11. A) Normalised z-velocity magnitude distribution and b) radial z-velocity magnitude of the 300–500 µm and 500–700 µm cases.

cleaning the scanned geometries, the resulting beds are progressively deformed, exhibiting changes in both their porosity (bulk, radial, and axial) and their interparticle network (pore size, coordination number) characteristics. Aside from image-processing, by segmenting the particles from their neighbours to treat contact regions and to generate a good quality mesh, the meshing process further reduces the bed volume.

The hydrodynamic profiles, i.e., the X-, Y- and Z-velocity magnitudes and the pressure drop, of the produced beds were then examined. The highly poly-dispersed nature of the catalytic beds resulted in large local changes in the Z-velocity magnitude, with the maximum velocity magnitude being 16-times higher than the average Z-velocity within the bed. Moreover, deformations in small topological features were observed to introduce significant errors in the hydrodynamic behaviour. A particle size study revealed that larger particles form a less tightly packed bed with larger interparticle pores, which increase the permeability of the medium, thus reducing local velocity magnitudes and the pressure drop experienced by the flow. Throughout this study, the local 3D interconnectivity of the pores was identified as an equally important structural parameter as the local porosity of the bed. This revealed an interconnection between the bed structure and its hydrodynamic profile that was previously neglected, leading to key insights into further CFD model development and reactor optimisation.

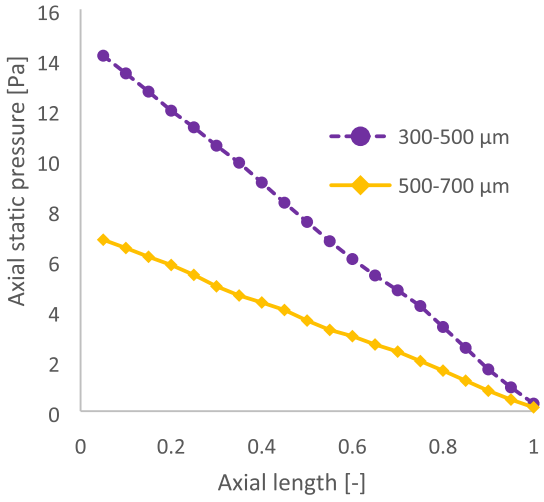

Fig. 12. Axial static pressure drop of the 300–500 and 500–700 µm bed cases.

Table 5
Exposed surface area and residence time of the 300–500 and 500–700 µm cases.

	Exposed surface area [cm^2]	Residence time [ms]		
		Min	Max	Average
300–500 µm	4.01	45	85	71
500–700 µm	2.81	47	101	75

Declaration of Competing Interest

The authors declare the following financial interests/personal relationships which may be considered as potential competing interests: Stylianos Kyrimis reports financial support was provided by the Industrial Decarbonisation Research and Innovation Centre (IDRIC), grant number EP/V027050/1.

Acknowledgements

The authors would like to thank the Industrial Decarbonisation Research and Innovation Centre (IDRIC), grant number EP/V027050/1, for their funding. In addition, the authors would like to acknowledge the use of the IRIDIS 5 High Performance Computing Facility, and associated support services at the University of Southampton, in the completion of this work. Finally, we would like to thank Kathryn E. Rankin and Siul Ruiz for their help with Simpleware and geometry meshing.

Appendix A. Supplementary data

Supplementary data to this article can be found online at https://doi.org/10.1016/j.apt.2023.104199.

References

[1] International Energy Agency (IEA), "Achieving Net Zero Heavy Industry Sectors in G7 members," Paris, 2022. [Online]. Available: https://www.iea.org/reports/achieving-net-zero-heavy-industry-sectors-in-g7-members.

[2] International Energy Agency (IEA), "Net Zero by 2050," Paris, 2021. [Online]. Available: https://www.iea.org/reports/net-zero-by-2050.

[3] International Energy Agency (IEA), "CO2 Emissions in 2022," Paris, 2023. [Online]. Available: https://www.iea.org/reports/co2-emissions-in-2022.

[4] G. Hutchings et al., Sustainable synthetic carbon based fuels for transport, Policy Briefing, The Royal Society, London, 2019/9/20.

[5] G. Bozzano, F. Manenti, Efficient methanol synthesis: Perspectives, technologies and optimization strategies, Prog. Energy Combust. Sci. vol. 56 (2016) 71–105, https://doi.org/10.1016/j.pecs.2016.06.001.

[6] M. Zhang, Y. Yu, Dehydration of Ethanol to Ethylene, Ind. Eng. Chem. Res. 52 (28) (2013) 9505–9514, https://doi.org/10.1021/ie401157c.

[7] Ronald W. Missen, Charles A. Mims, B.A. Saville, Introduction to Chemical Reaction Engineering and Kinetics. Wiley, 1999.

[8] B. Partopour, A.G. Dixon, 110th Anniversary: Commentary: CFD as a Modeling Tool for Fixed Bed Reactors, Ind. Eng. Chem. Res. 58 (14) (2019) 5733–5736, https://doi.org/10.1021/acs.iecr.8b06380.

[9] A.G. Dixon, M. Nijemeisland, E.H. Stitt, Packed Tubular Reactor Modeling and Catalyst Design using Computational Fluid Dynamics, Computational Fluid Dynamics 31 (2006) 307–389, https://doi.org/10.1016/s0065-2377(06)31005-8.

[10] A.G. Dixon, M. Nijemeisland, CFD as a Design Tool for Fixed-Bed Reactors, Ind. Eng. Chem. Res. 40 (23) (2001) 5246–5254, https://doi.org/10.1021/ie001035a.

[11] G.E. Mueller, Numerically packing spheres in cylinders, Powder Technol. 159 (2) (2005) 105–110, https://doi.org/10.1016/j.powtec.2005.06.002.

[12] J. Theuerkauf, P. Witt, D. Schwesig, Analysis of particle porosity distribution in fixed beds using the discrete element method, Powder Technol. 165 (2) (2006) 92–99, https://doi.org/10.1016/j.powtec.2006.03.022.

[13] J. von Seckendorff, O. Hinrichsen, Review on the structure of random packed-beds, Can. J. Chem. Eng. 99 (S1) (2021) S703–S733, https://doi.org/10.1002/cjce.23959.

[14] C. Shin, Tortuosity correction of Kozeny's hydraulic diameter of a porous medium, Phys. Fluids 29 (2) (2017), https://doi.org/10.1063/1.4976550.

[15] X. Zhou, Y. Duan, X. Huai, X. Li, 3D CFD modeling of acetone hydrogenation in fixed bed reactor with spherical particles, Particuology 11 (6) (2013) 715–722, https://doi.org/10.1016/j.partic.2012.10.009.

[16] S. Das, N.G. Deen, J.A.M. Kuipers, A DNS study of flow and heat transfer through slender fixed-bed reactors randomly packed with spherical particles, Chem. Eng. Sci. 160 (2017) 1–19, https://doi.org/10.1016/j.ces.2016.11.008.

[17] H. Bai, J. Theuerkauf, P.A. Gillis, P.M. Witt, A Coupled DEM and CFD Simulation of Flow Field and Pressure Drop in Fixed Bed Reactor with Randomly Packed Catalyst Particles, Ind. Eng. Chem. Res. 48 (8) (2009) 4060–4074, https://doi.org/10.1021/ie801548h.

[18] G.D. Wehinger, C. Fütterer, M. Kraume, Contact Modifications for CFD Simulations of Fixed-Bed Reactors: Cylindrical Particles, Ind. Eng. Chem. Res. 56 (1) (2017) 87–99, https://doi.org/10.1021/acs.iecr.6b03596.

[19] G.R. George, M. Bockelmann, L. Schmalhorst, D. Beton, A. Gerstle, A. Lindermeir, G.D. Wehinger, Radial heat transport in a fixed-bed reactor made of metallic foam pellets: Experiment and particle-resolved computational fluid dynamics, Int. J. Heat Mass Transf. 197 (2022), https://doi.org/10.1016/j.ijheatmasstransfer.2022.123376.

[20] N. Jurtz, G.D. Wehinger, U. Srivastava, T. Henkel, M. Kraume, Validation of pressure drop prediction and bed generation of fixed-beds with complex particle shapes using discrete element method and computational fluid dynamics, AIChE J 66 (6) (2020) e16967.

[21] B. Partopour, A.G. Dixon, An integrated workflow for resolved-particle packed bed models with complex particle shapes, Powder Technol. 322 (2017) 258–272, https://doi.org/10.1016/j.powtec.2017.09.009.

[22] Q. Chang, L. Yang, W. Ge, Fluid-particle heat transfer in static assemblies: Effect of particle shape, Int. J. Heat Mass Transf. 166 (2021), https://doi.org/10.1016/j.ijheatmasstransfer.2020.120730.

[23] P. Niegodajew, K. Gruszka, M. Marek, Numerical study of cylindrical particles' orientation in narrow packed beds, Powder Technol. 386 (2021) 528–539, https://doi.org/10.1016/j.powtec.2021.03.069.

[24] G.M. Karthik, V.V. Buwa, Effect of particle shape on fluid flow and heat transfer for methane steam reforming reactions in a packed bed, AIChE J 63 (1) (2017) 366–377, https://doi.org/10.1002/aic.15542.

[25] M.V. Tabib, S.T. Johansen, S. Amini, A 3D CFD-DEM Methodology for Simulating Industrial Scale Packed Bed Chemical Looping Combustion Reactors, Ind. Eng. Chem. Res. 52 (34) (2013) 12041–12058, https://doi.org/10.1021/ie302028s.

[26] A. Pavlišič, R. Ceglar, A. Pohar, B. Likozar, Comparison of computational fluid dynamics (CFD) and pressure drop correlations in laminar flow regime for packed bed reactors and columns, Powder Technol. 328 (2018) 130–139, https://doi.org/10.1016/j.powtec.2018.01.029.

[27] S.J. Rodrigues, N. Vorhauer-Huget, T. Richter, E. Tsotsas, Influence of Particle Shape on Tortuosity of Non-Spherical Particle Packed Beds, Processes, 11(1) (2023) 3. [Online]. Available: https://www.mdpi.com/2227-9717/11/1/3.

[28] K.G. Manoharan, V.V. Buwa, A computational approach for the selection of optimal catalyst shape for solid-catalysed gas-phase reactions, React. Chem. Eng. 5 (1) (2020) 163–182.

[29] M. Zhang, H. Dong, Z. Geng, Computational study of particle packing process and fluid flow inside Polydisperse cylindrical particles fixed beds, Powder Technol. 354 (2019) 19–29, https://doi.org/10.1016/j.powtec.2019.05.061.

[30] G. Boccardo, F. Augier, Y. Haroun, D. Ferré, D.L. Marchisio, Validation of a novel open-source work-flow for the simulation of packed-bed reactors, Chem. Eng. J. 279 (2015) 809–820, https://doi.org/10.1016/j.cej.2015.05.032.

[31] R. Caulkin, X. Jia, C. Xu, M. Fairweather, R.A. Williams, H. Stitt, M. Nijemeisland, S. Aferka, M. Crine, A. Léonard, D. Toye, P. Marchot, Simulations of Structures in Packed Columns and Validation by X-ray Tomography, Ind. Eng. Chem. Res. 48 (1) (2009) 202–213.

[32] P. Lovreglio, S. Das, K.A. Buist, E.A.J.F. Peters, L. Pel, J.A.M. Kuipers, Experimental and numerical investigation of structure and hydrodynamics in packed beds of spherical particles, AIChE J 64 (5) (2018) 1896–1907, https://doi.org/10.1002/aic.16127.

[33] B. Manz, L.F. Gladden, P.B. Warren, Flow and dispersion in porous media: Lattice-Boltzmann and NMR studies, AIChE J 45 (9) (1999) 1845–1854, https://doi.org/10.1002/aic.690450902.

[34] M.J. Baker, P.G. Young, G.R. Tabor, Image based meshing of packed beds of cylinders at low aspect ratios using 3d MRI coupled with computational fluid dynamics, Comput. Chem. Eng. 35 (10) (2011) 1969–1977, https://doi.org/10.1016/j.compchemeng.2011.03.017.

[35] M.D. Mantle, A.J. Sederman, L.F. Gladden, Single- and two-phase flow in fixed-bed reactors: MRI flow visualisation and lattice-Boltzmann simulations, Chem. Eng. Sci. 56 (2) (2001) 523–529, https://doi.org/10.1016/S0009-2509(00)00256-6.

[36] E.N. Landis, D.T. Keane, X-ray microtomography, Mater. Charact. 61 (12) (2010) 1305–1316, https://doi.org/10.1016/j.matchar.2010.09.012.

[37] M. Suzuki, T. Shinmura, K. Iimura, M. Hirota, Study of the Wall Effect on Particle Packing Structure Using X-ray Micro Computed Tomography, Adv. Powder Technol. 19 (2) (2008) 183–195, https://doi.org/10.1163/156855208X293817.

[38] B.-H. Yang, A.-X. Wu, X.-X. Miao, J.-Z. Liu, 3D characterization and analysis of pore structure of packed ore particle beds based on computed tomography images, Trans. Nonferrous Met. Soc. Chin. 24 (3) (2014) 833–838, https://doi.org/10.1016/S1003-6326(14)63131-9.

[39] W.A.M. Fernando, I.M.S.K. Ilankoon, A. Rabbani, M. Yellishetty, Inter-particle fluid flow visualisation of larger packed beds pertaining to heap leaching using X-ray computed tomography imaging, Miner. Eng. 151 (2020), https://doi.org/10.1016/j.mineng.2020.106334.

[40] W. Zhang, K.E. Thompson, A.H. Reed, L. Beenken, Relationship between packing structure and porosity in fixed beds of equilateral cylindrical particles, Chem. Eng. Sci. 61 (24) (2006) 8060–8074, https://doi.org/10.1016/j.ces.2006.09.036.

[41] N. Jurtz, M. Kraume, G.D. Wehinger, Advances in fixed-bed reactor modeling using particle-resolved computational fluid dynamics (CFD), Reviews in Chemical Engineering, vol. 35, no. 2, pp. 139-190, 2019, doi: doi:10.1515/revce-2017-0059.

[42] T. Atmakidis, E.Y. Kenig, CFD-based analysis of the wall effect on the pressure drop in packed beds with moderate tube/particle diameter ratios in the laminar flow regime, 155(1-2) (2009) 404-410, doi: 10.1016/j.cej.2009.07.057.

[43] W. Peng, M. Xu, X. Huai, Z. Liu, 3D CFD simulations of acetone hydrogenation in randomly packed beds for an isopropanol–acetone–hydrogen chemical heat pump, Appl. Therm. Eng. 94 (2016) 238–248, https://doi.org/10.1016/j.applthermaleng.2015.10.130.

[44] A.G. Dixon, Local transport and reaction rates in a fixed bed reactor tube: Exothermic partial oxidation of ethylene, Chem. Eng. Sci. 231 (2021), https://doi.org/10.1016/j.ces.2020.116305.

[45] A.G. Dixon, Local transport and reaction rates in a fixed bed reactor tube: Endothermic steam methane reforming, Chem. Eng. Sci. 168 (2017) 156–177, https://doi.org/10.1016/j.ces.2017.04.039.

[46] T. Eppinger, K. Seidler, M. Kraume, DEM-CFD simulations of fixed bed reactors with small tube to particle diameter ratios, Chem. Eng. J. 166 (1) (2011) 324–331, https://doi.org/10.1016/j.cej.2010.10.053.

[47] G.D. Wehinger, T. Eppinger, M. Kraume, Detailed numerical simulations of catalytic fixed-bed reactors: Heterogeneous dry reforming of methane, Chem. Eng. Sci. 122 (2015) 197–209, https://doi.org/10.1016/j.ces.2014.09.007.

[48] A.G. Dixon, M. Nijemeisland, E.H. Stitt, Systematic mesh development for 3D CFD simulation of fixed beds: Contact points study, Comput. Chem. Eng. 48 (2013) 135–153, https://doi.org/10.1016/j.compchemeng.2012.08.011.

[49] M. Sadeghi, M. Mirdrikvand, G.R. Pesch, W. Dreher, J. Thöming, Full-field analysis of gas flow within open-cell foams: comparison of micro-computed tomography-based CFD simulations with experimental magnetic resonance flow mapping data, Exp. Fluids 61 (5) (2020) 124, https://doi.org/10.1007/s00348-020-02960-4.

[50] P. Ranut, E. Nobile, L. Mancini, High resolution microtomography-based CFD simulation of flow and heat transfer in aluminum metal foams, Appl. Therm. Eng. 69 (1) (2014) 230–240, https://doi.org/10.1016/j.applthermaleng.2013.11.056.

[51] X. Fan, X. Ou, F. Xing, G.A. Turley, P. Denissenko, M.A. Williams, N. Batail, C. Pham, A.A. Lapkin, Microtomography-based numerical simulations of heat transfer and fluid flow through β-SiC open-cell foams for catalysis, Catal. Today 278 (2016) 350–360.

[52] S. Kyrimis, K.E. Rankin, M.E. Potter, R. Raja, L.-M. Armstrong, Towards realistic characterisation of chemical reactors: An in-depth analysis of catalytic particle beds produced by sieving, Adv. Powder Technol. 34 (2) (2023), https://doi.org/10.1016/j.apt.2022.103932.

[53] S. Kyrimis, Robert Raja, L.-M. Armstrong, Hydrodynamic profiles of computed tomography-scanned polydispersed beds produced by sieving, in: Proceedings of the 10th International Conference on Fluid Flow, Heat and Mass Transfer (FFHMT '23), 2023, doi: 10.11159/ffhmt23.171.
[54] J. Schindelin, I. Arganda-Carreras, E. Frise, V. Kaynig, M. Longair, T. Pietzsch, S. Preibisch, C. Rueden, S. Saalfeld, B. Schmid, J.-Y. Tinevez, D.J. White, V. Hartenstein, K. Eliceiri, P. Tomancak, A. Cardona, Fiji: an open-source platform for biological-image analysis, Nat. Methods 9 (7) (2012) 676–682.
[55] A.N. Houston, W. Otten, R. Falconer, O. Monga, P.C. Baveye, S.M. Hapca, Quantification of the pore size distribution of soils: Assessment of existing software using tomographic and synthetic 3D images, Geoderma 299 (2017) 73–82, https://doi.org/10.1016/j.geoderma.2017.03.025.
[56] A. Rabbani, S. Jamshidi, S. Salehi, An automated simple algorithm for realistic pore network extraction from micro-tomography images, J. Pet. Sci. Eng. 123 (2014) 164–171, https://doi.org/10.1016/j.petrol.2014.08.020.
[57] T.G. Baychev, A.P. Jivkov, A. Rabbani, A.Q. Raeini, Q. Xiong, T. Lowe, P.J. Withers, Reliability of Algorithms Interpreting Topological and Geometric Properties of Porous Media for Pore Network Modelling, Transp. Porous Media 128 (1) (2019) 271–301.
[58] ThermoFisher Scientific., Avizo Software User's Guide, Avizo Software User's Guide, 2019.
[59] S. Kyrimis, M.E. Potter, R. Raja, L.-M. Armstrong, Understanding catalytic CO 2 and CO conversion into methanol using computational fluid dynamics, Faraday Discuss. 230 (2021) 100–123.
[60] A.G. Dixon, M.E. Taskin, M. Nijemeisland, E.H. Stitt, CFD Method To Couple Three-Dimensional Transport and Reaction inside Catalyst Particles to the Fixed Bed Flow Field, Ind. Eng. Chem. Res. 49 (19) (2010) 9012–9025, https://doi.org/10.1021/ie100298q.
[61] ANSYS Inc., ANSYS Fluent User's Guide, Fluent User's Guide, vol. Release 15.0, November 2013.
[62] Y. Zhang, Y. Ding, P.D. Christofides, Multiscale computational fluid dynamics modeling of thermal atomic layer deposition with application to chamber design, Chem. Eng. Res. Des. 147 (2019) 529–544, https://doi.org/10.1016/j.cherd.2019.05.049.
[63] ANSYS Inc., ANSYS Fluent Theory Guide, Fluent Theory Guide, vol. Release 15.0, November 2013 2013.
[64] S. Kyrimis, R. Robert, and L.-M. Armstrong, Quantifying the impact of intraparticle convection within fixed beds formed by catalytic particles with low macro-porosities, ACS Engineering Au (Under review), 2023.
[65] B. Ghanbarian, A.G. Hunt, R.P. Ewing, M. Sahimi, Tortuosity in Porous Media: A Critical Review, Soil Sci. Soc. Am. J. 77 (5) (2013) 1461–1477, https://doi.org/10.2136/sssaj2012.0435.
[66] Y. Jin, X. Li, M. Zhao, X. Liu, H. Li, A mathematical model of fluid flow in tight porous media based on fractal assumptions, Int. J. Heat Mass Transf. 108 (2017) 1078–1088, https://doi.org/10.1016/j.ijheatmasstransfer.2016.12.096.
[67] R.E. Hayes, A. Afacan, B. Boulanger, An equation of motion for an incompressible Newtonian fluid in a packed bed, 18(2) (1995) 185-198, doi: 10.1007/bf01064677.
[68] H. Freund, J. Bauer, T. Zeiser, G. Emig, Detailed Simulation of Transport Processes in Fixed-Beds, Ind. Eng. Chem. Res. 44 (16) (2005) 6423–6434, https://doi.org/10.1021/ie0489453.
[69] V. Spallina, P. Chiesa, E. Martelli, F. Gallucci, M.C. Romano, G. Lozza, M. van Sint Annaland, Reactor design and operation strategies for a large-scale packed-bed CLC power plant with coal syngas, Int. J. Greenhouse Gas Control 36 (2015) 34–50.
[70] B. Yang, T. Yang, Z. Xu, H. Liu, X. Yang, W. Shi, Impact of Particle-Size Distribution on Flow Properties of a Packed Column, J. Hydrol. Eng. 24 (3) (2019) 04018070, https://doi.org/10.1061/(asce)he.1943-5584.0001735.
[71] B. Partopour, A.G. Dixon, Integrated multiscale modeling of fixed bed reactors: Studying the reactor under dynamic reaction conditions, Chem. Eng. J. 377 (2019), https://doi.org/10.1016/j.cej.2018.08.124.
[72] S.H. Fogler, Elements of Chemical Reaction Engineering, fifth ed., Pearson, 2016.